The fully-automatic Sentinel-1 Global Flood Monitoring service: Scientific challenges and future directions

Wolfgang Wagner[a,b], Bernhard Bauer-Marschallinger[a], Florian Roth[a], Tobias Stachl[b], Christoph Reimer[b], Niall McCormick[c], Patrick Matgen[d], Marco Chini[d], Yu Li[d], Sandro Martinis[e], Marc Wieland[e], Franziska Kraft[e], Davide Festa[a], Muhammed Hassaan[a], Mark Edwin Tupas[a,f], Jie Zhao[a,g], Michaela Seewald[h], Michael Riffler[h], Luca Molini[i], Richard Kidd[b], Christian Briese[b], Peter Salamon[c]

[a] *Technische Universität Wien, Department of Geodesy and Geoinformation, Vienna, Austria*
[b] *EODC Earth Observation Data Centre, Vienna, Austria*
[c] *European Commission, Joint Research Centre, Ispra, Italy*
[d] *Luxembourg Institute of Science and Technology, Esch-Belval Belvaux Sanem, Luxemburg*
[e] *Deutsches Zentrum für Luft- und Raumfahrt, Weßling, Germany*
[f] *University of the Philippines, Department of Geodetic Engineering, Quezon City, Philippines*
[g] *Technical University of Munich, Munich, Germany*
[h] *GeoVille Information Systems and Data Processing, Innsbruck, Austria*
[i] *Centro Internazionale in Monitoraggio Ambientale, Savona, Italy*

Abstract

One of the critical factors in operational satellite-based flood monitoring efforts is the time it takes from the acquisition of the satellite image to the delivery of the flood maps to users. Any human involvement, such as coordinating satellite acquisitions or manually interpreting images, can delay this process. To avoid such delays, a fundamentally new approach was adopted for the Sentinel-1 based Global Flood Monitoring (GFM) service: All Synthetic Aperture Radar (SAR) images acquired by the Sentinel-1 satellites in VV polarisation over land are processed entirely automatically, enabling flood maps to be delivered within eight hours of acquisition. The flood maps, along with a novel flood likelihood layer, are generated using ensemble approaches that integrate three complementary flood mapping algorithms along with reference water maps to distinguish flooded areas from permanent and seasonal water bodies. A notable feature of the service is its capability not only to

depict flood-pixels evident in the Sentinel-1 images but also to provide contextual information that identifies areas where flood mapping is not feasible or problematic due to land cover and environmental conditions. These advancements were made possible through the use of a global 20 m backscatter datacube, which has enabled the characterisation of the backscatter behaviour for approximately 379 billion land surface pixels and deriving the reference water maps and a global flood archive. The GFM service was launched in 2021 as a new component of the Copernicus Emergency Management Service (CEMS) and has quickly garnered attention from users worldwide. In this review, we offer the first comprehensive overview of the scientific accomplishments and challenges faced during the first three years of operations. This analysis discloses discrepancies between the current service capabilities and the requirements of operational users, and provides directions for future research and service improvements, anticipating the increasing availability of systematic SAR data coverage from ROSE-L and other future SAR missions.

Keywords: Flood monitoring, Inland water, Sentinel-1, SAR, Datacube, Copernicus

1. Introduction

1.1. Satellite-based flood monitoring

Significant efforts have been made over the past years to improve flood risk management. European and global policy frameworks such as the Floods Directive of the European Union and the Sendai Framework for Disaster Risk Reduction have enabled the strengthening of prevention, preparedness, and response to floods. While this has resulted in a decrease in flood fatalities and economic losses for Europe (Paprotny et al., 2018), this is not true for other regions of the world. In addition, the increase in weather and climate related extremes thwarts the achievements in flood risk management. According to the Intergovernmental Panel on Climate Change (IPCC), human-caused climate change is already affecting many weather and climate extremes including floods in every region across the globe (Calvin et al., 2023). The recent large-scale floods in central Europe in mid-September 2024, which were caused by record-breaking rainfall over a period of four days, have demonstrated again the increasing challenges that civil protection and emergency responders are facing in order to reduce the impacts of floods on our society and economy (Kimutai et al., 2024).

With the increasing availability of satellite imagery, particularly through Europe's Earth observation programme Copernicus, satellite-based flood monitoring has become a crucial tool for flood response. It offers a rapid and efficient overview of flood situations, especially for large-scale flood events. As part of the Copernicus Emergency Management Service (CEMS), satellite imagery is routinely used to generate flood maps within hours or days, following activation by authorised users from European Member States and other countries participating in the European Civil Protection Mechanism (Denis et al., 2016). The on-demand CEMS Rapid Mapping service operates 24/7, providing geospatial information on the impact of selected disasters worldwide using both optical and radar satellite images (Ajmar et al., 2017). In this paper, we present CEMS's new Global Flood Monitoring (GFM) component, which provides in near real-time, continuously, and fully automatically, flood maps together with contextual auxiliary layers.

1.2. Systematic observation capabilities of Sentinel-1

The potential of SAR sensors for flood mapping has been recognised since the inception of spaceborne SAR missions in the second half of the 20th century. Following the launch of Seasat in 1978, the first civil satellite equipped with an L-band SAR sensor, researchers started exploring the data for flood mapping and water resources evaluation (Imhoff et al., 1987). SAR technology is particularly effective in detecting surface water features under cloudy conditions, thanks to its ability to penetrate the atmosphere at microwave frequencies and the contrasting return signals from smooth water surfaces compared to rough terrain (Lewis, 1998). This capability allows SAR to overcome the limitations posed by cloud cover, which often obscures visibility for optical satellite systems, particularly during the initial phases of a flood. Consequently, Imhoff et al. (1987) predicted that SAR would become a powerful tool for measuring and monitoring flood progression as satellite-acquired SAR imagery becomes available worldwide in the 1990s.

This prediction turned out to be only partially true. While the first generation of SAR satellites launched in the 1990s, including ERS-1 and ERS-2 from Europe, JERS-1 from Japan, and Radarsat from Canada, enabled numerous scientific studies that investigated algorithms for extracting flood extent (Oberstadler et al., 1997; Wang, 2004), their impact on real-world flood monitoring efforts was limited. The problem was not the quality of the data, which was excellent for a first-generation technology (Meadows et al.,

2001), but rather data availability. Essentially, due to the lack of frequent observations, one had to be "fortunate" to obtain a high-resolution SAR image of a flood (Kiage et al., 2005). This had technical and organisational reasons. The main technical constraints stem from fixed satellite orbits and the high energy demand of high-resolution SAR imaging modes. Space agencies tried to mitigate these restrictions by developing SAR instruments with multiple imaging modes that enable the acquisition of SAR images with varying spatial extents, resolutions, and incidence angles (Raney et al., 1991). Consequently, users had to select and request appropriate SAR images several days in advance of acquisitions, which is very problematic, particularly for flood mapping applications.

Improving data availability during flood situations can be accomplished through various strategies. The most straightforward solution is to gather data from as many SAR (and optical) satellites as possible (Voigt et al., 2007), a concept supported by the International Charter on Space and Major Disasters. This strategy is gaining momentum with the deployment of large fleets of small, programmable SAR satellites, as seen with new commercial SAR data providers (Ignatenko et al., 2024). A crucial component for the success of this strategy is to have advance knowledge of the locations requiring data collection. This can be facilitated by leveraging hydrological model predictions (Boni et al., 2016; Wania et al., 2021) and monitoring social media posts (Rossi et al., 2018). An alternative strategy is to develop SAR missions that provide frequent high-resolution coverage without the need for programming-specific image acquisitions. This was the road chosen for the Sentinel-1 mission. Instead of offering many different imaging modes like its predecessors, Sentinel-1 was developed to operate in a limited number of pre-programmed, conflict-free modes, allowing for high-resolution imaging of the Earth's surface with extended swath width and duty cycles (Torres et al., 2012). Additionally, from the outset, Sentinel-1 acquisitions have been scheduled according to a stable and predefined observation scenario, with sufficient resource margin to flexibly handle emergency requests (Potin et al., 2012). The duty cycle, which determines the sensor's effective ground coverage per orbit revolution, is probably one of the most overlooked SAR mission characteristics. With a duty cycle of 28 min and a swath width of up to 250 km, even a single Sentinel-1 satellite achieves a daily global coverage unmatched by any of its predecessors or small SAR satellite swarms. For the Sentinel-1 Next Generation, the duty cycle will be further extended to approximately 38 min and the swath width to 400 km (Torres et al., 2024).

Sentinel-1 was developed as a constellation of two SAR satellites flying in a near-polar sun-synchronous orbit with a 12-day repeat cycle (i.e. the time between two successive identical orbits). Together, the two satellites achieve a combined orbit repeat cycle of 6 days. The first two satellites, Sentinel-1A and Sentinel-1B, were launched in April 2014 and April 2016, respectively. Unfortunately, Sentinel-1B failed prematurely in December 2021. Sentinel-1C was launched in December 2024 and Sentinel-1D will follow in 2025. The principle Sentinel-1 acquisition mode over land is the Interferometric Wide (IW) swath mode, which captures three sub-swaths using an advanced ScanSAR technique introduced by De Zan and Monti Guarnieri (2006). This results in 250 km wide images with a spatial resolution of approximately 3 m in range and 22 m in azimuth directions (single look). The on-board SAR sensor can emit and receive polarized electromagnetic waves along both vertical (V) and horizontal (H) planes. The base configuration over land is to collect IW imagery in VV and VH polarisation. According to the Copernicus Sentinel Data Access Annual Report 2023, the Sentinel-1 mission produces up to 6 terabytes daily and the delivery time of near-real-time products can be as fast as 1 hour after data acquisition. The average revisit time (i.e. the time between two subsequent images of the same area, which may be observed from different orbits) of two Sentinel-1 satellites is illustrated in Fig. 1, based on all IW images acquired by Sentinel-1A and Sentinel-1B from 2016 to 2021. Europe is covered best, with revisit times ranging from 1 to 3 days. For other priority regions, as outlined in the observation scenario, the average revisit time is between 4 and 6 days. Most other land areas are observed every 6 to 12 days, although some individual orbits covering high-latitude regions, Africa, islands, and coastal regions have even longer revisit intervals.

< Fig. 1 >

1.3. SAR-based flood mapping

Flood mapping is among the first and most important applications of spaceborne SAR missions (Amitrano et al., 2024). Most flood mapping studies start from the premise that backscatter from water surfaces is lower than that from surrounding land. Consequently, many algorithms concentrate on detecting areas of low backscatter within individual SAR images. Assuming that all detected areas represent water surfaces, flood extent is obtained by subtracting permanent water bodies (Twele et al., 2016; Rahman and

Thakur, 2018). The techniques used for mapping water surfaces are diverse, ranging from multi-scale thresholding methods to fuzzy classifiers and deep learning approaches, often enhanced by post-processing steps for image improvement (Bentivoglio et al., 2022; Amitrano et al., 2024). While these algorithms generally perform well under ideal conditions, various physical factors can disrupt the assumption that backscatter from flooded areas is consistently low while that from land is higher. Some effects can even completely obstruct the detection of flooded areas.

The physical mechanism responsible for the high contrast in radar imagery between flooded and non-flooded terrain is the specular, mirror-like reflection of SAR signals from smooth water surfaces, which produces very low backscattered amplitude. However, various factors – wind, rain, variable water depths, and obstacles obstructing water flow – can induce ripples and waves on the water surface that significantly increase backscatter (Dasgupta et al., 2018). Additionally, vegetation and other objects that extend above the water's surface can increase backscatter due to direct scattering from these objects and double bounce effects occurring between the water surface and the scattering elements. In these situations, the contrast between flooded and non-flooded areas may lessen or disappear entirely. When double bounce effects are pronounced, it may even be possible to identify flooded vegetation and urban regions by detecting very strong backscatter echoes (Tsyganskaya et al., 2018; Mason et al., 2014).

Even when backscatter from the water surface is low, confusion can arise with water-free land areas that also appear dark in SAR images (Lewis, 1998; Zhang et al., 2020). These water-lookalike areas include sandy (beaches, sand dunes, etc.) and paved (airport runways, parking lots, etc.) surfaces, which have a smooth texture at radar wavelengths, resulting in consistently low backscatter throughout the year. Other land surfaces may exhibit low backscatter only during specific seasons or environmental conditions, such as when the soils and vegetation are dry, frozen or covered by wet snow (Pulvirenti et al., 2014). Additionally, SAR imagery exhibits dark, noisy patches in radar shadow regions. All these water-lookalike areas contribute to ambiguities in SAR image classification, leading to false alarms. Such false alarms can be removed in sloping terrain by using topographic indices that derive drainage patterns or valley bottoms from digital elevation models (DEMs) (Huang et al., 2017). In flood mapping, probably the most widely used terrain index is the Height Above Nearest Drainage (HAND) index, which expresses the height difference between a DEM cell and the closest cell

of the drainage network along the actual flow path (Rennó et al., 2008).

Another, more important way to reduce false alarms is to employ change detection techniques that compare a SAR image acquired during the flood with a reference SAR image depicting non-flooded conditions (Carincotte et al., 2006; Giustarini et al., 2013; Long et al., 2014). The assumption is that only SAR pixels showing a drop in backscatter value from the non-flood image to the flood image correspond to flooded areas. In addition to minimising the false alarm rate, change detection techniques simplify the process of establishing thresholds that are effective across various environments and weather conditions (Tupas et al., 2023b), and they eliminate the need for external datasets to delineate permanent water surfaces. However, one challenge is to select suitable SAR reference images that best represent 'normal' conditions (Hostache et al., 2012). Furthermore, change detection does not solve the problem of underdetection in case the backscatter from the flooded areas is elevated due to a rough water surface, emergent vegetation, or buildings.

In their review of SAR-based flood monitoring, Amitrano et al. (2024) highlight that monitoring floods in vegetated and urban areas still presents significant challenges due to the complex scattering mechanisms that impede accurate water region extraction. They recommend employing multi-dimensional SAR data (e.g. multi-phase, multi-polarisation, multi-frequency) to isolate the different scattering mechanisms that contribute to the overall received signal. Furthermore, the thematic accuracy of flood mapping algorithms is often enhanced through the integration of ancillary datasets, such as land cover information (Wang et al., 2022), radar shadow masks (Rees, 2000), and topographic indices (Tupas et al., 2023a). Beyond improving mapping accuracy, multi-dimensional SAR data and ancillary datasets play a crucial role in estimating retrieval uncertainties and delineating exclusion areas where the presence of water simply cannot be determined from SAR backscatter observations due to physical reasons (Zhao et al., 2021a), as is, for example, the case in tropical forest regions (Carreno-Luengo et al., 2024).

1.4. Scope of the flood monitoring service and this review

As noted by Solbo and Solheim already in 2004, operational flood monitoring services require fully-automated methods capable of processing available SAR data in near real-time (NRT). One of the pioneering studies that investigated the use of Sentinel-1 SAR data for NRT flood mapping was conducted by Twele et al. (2016). They demonstrated that, without requiring

user intervention at any stage of the flood mapping process, time-sensitive disaster information could be produced in less than 45 min after a new dataset was made available on one of the Sentinel data hubs. Recognising the unique opportunities presented by such NRT capabilities to enhance the timeliness of information during emergencies, the European Commission initiated a feasibility study for an automated, global, satellite-based flood monitoring product. The main conclusion of this feasibility study was that state-of-the-art, scientific methods for automatically detecting and identifying flood events are mature and ready for operational implementation for Sentinel-1 (Matgen et al., 2019). Following the study's recommendations on the design of the data processing architecture and system requirements (Wagner et al., 2020), a fully automatic global Sentinel-1 processing system was set up in less than a year and put into operations at the end of 2021 (Salamon et al., 2021). This so-called Global Flood Monitoring (GFM) service is a new and independent component of CEMS, complementing its flood early warnings and on-demand mapping services (Matthews et al., 2025b; Denis et al., 2016). All worldwide GFM flood data are freely available in NRT, as well as the historic data from an archive covering the complete Sentinel-1 observation period (from 2015 to present).

The CEMS GFM service is designed to provide continuous global flood monitoring by automatically processing and analysing all incoming Sentinel-1 IW images over ice-free land. For cost reasons, the service utilises so far only one polarisation of the IW images. VV polarisation was selected over VH polarisation because studies have shown that VV polarisation offers slightly higher thematic accuracy compared to VH polarisation (Twele et al., 2016). When there are no delays in the provision of Sentinel-1 data on the Copernicus data hubs, users can expect 20 m resolution flood maps within 8 h after image acquisition. The service employs three independently developed flood mapping algorithms to enhance the robustness and accuracy of flood and water extent maps, and to build a high degree of redundancy into the service. To assist users in interpreting the GFM data, the products do not just contain binary flood maps but also flood likelihood values and detailed contextual information, including data layers showing permanent and seasonal water bodies, environmental conditions that may affect the quality of the flood information, and exclusion areas where Sentinel-1 is unable to provide flood data.

In terms of the data processing efforts alone – without even considering the complexity of the scientific algorithms – the CEMS GFM service stands

out as the largest systematic initiative for operational SAR-based flood monitoring. Other SAR-based systems typically focus on specific regions, lack transparency, or still require some degree of user interaction to start SAR data processing. For instance, Ohki et al. (2024) recently introduced the first ALOS-2-based algorithms designed for rapid and automated flood detection in Japan. Efforts to create regional-scale Sentinel-1-based flood monitoring capabilities have often leveraged the Google Earth Engine (GEE), which has emerged as a powerful web platform for managing large satellite datasets efficiently (Velastegui-Montoya et al., 2023). For example, DeVries et al. (2020) describe a method for NRT flood monitoring that combines contemporary SAR time series with historical Landsat data on the GEE, enabling rapid discrimination of floods and previously inundated areas. Tsyganskaya et al. (2018) present an advanced GEE solution by incorporating both ascending and descending passes, integrating slope and elevation parameters to reduce false positives in hilly terrains, and optimising on-the-fly processing to eliminate unnecessary computations.

The purpose of this paper is to give a comprehensive overview of the CEMS GFM service, discussing in Section 2 how the service was set up to benefit from novel scientific algorithms and Big Data solutions in a cloud platform environment. The service rests on a global Sentinel-1 backscatter datacube system that allows analysing the complete mission data archive for all continental land surface areas. After presenting results in Section 3, the technical and scientific challenges encountered during the first three years of operations are discussed in Section 4. Finally, in Section 5 we identify the main discrepancies between the current characteristics of the CEMS GFM service and user needs, and provide directions for scientific research and system development to enhance NRT flood monitoring capabilities.

2. Methods

2.1. Approach

The task of SAR-based flood mapping is commonly approached from an image classification perspective (Manavalan, 2017). In contrast, the CEMS GFM service treats it as a geophysical variable retrieval problem, similar to methodologies used for soil moisture (Quast et al., 2023) or biomass (Santoro and Cartus, 2018) retrievals. The key distinction is that image-oriented approaches focus on classifying water surfaces visible in SAR images, while

geophysical approaches emphasise the physical aspects of the problem, taking into account the sensitivity of backscatter measurements to the target variable under varying environmental conditions. This perspective calls for an accurate description of retrieval uncertainties accounting for both the visible and hidden components present within a SAR image. Consequently, the CEMS GFM service was designed not only to map flooded areas evident in the Sentinel-1 images but also to describe the associated uncertainties and exclusion cases. It achieves this by leveraging the information content of the Sentinel-1 time series and by fusing single-image, dual-image, and time series-based flood mapping algorithms using ensemble approaches. Additionally, contextual information layers are derived by combining Sentinel-1 data with ancillary datasets, such as surface water data, forest maps and a global settlement data set.

The GFM workflow is depicted in Fig. 2, illustrating the step-by-step generation of the GFM data products from the Sentinel-1 IW Ground Range Detected (GRD) images and ancillary data. The first step of the NRT workflow is to preprocess the GRD images, producing geometrically and radiometrically corrected images of the backscattering coefficient σ°. The σ° images are then ingested in a global Sentinel-1 datacube (Section 2.4.1) and forwarded to the three flood classification algorithms (Sections 2.2.1 to 2.2.3) and the advisory flag module (Section 2.3.3). After classifying each σ° image using the three complementary flood mapping algorithms, they are combined using two ensemble approaches that produce a binary flood map and a flood likelihood layer, respectively (Section 2.2.4). The NRT workflows utilises additional inputs that were derived offline by analysing the historic data within the Sentinel-1 datacube along with high-resolution ancillary datasets, namely a harmonic backscatter model required by the time series algorithm, monthly reference water maps (Section 2.3.1) and the exclusion mask (Section 2.3.2). In the following subsections, we examine the scientific literature and key arguments that influenced the design of the different algorithms and technical solutions. More detailed descriptions of each processing step and the associated technical specifications can be found on the Wiki pages of the GFM service (https://extwiki.eodc.eu/en/GFM). The Wiki pages also serve as a register of the changes made in the GFM implementation. This paper describes GFM version v3.2.0 released on 27^{th} November 2024.

< Fig. 2 >

2.2. Flood mapping algorithms

The three algorithms used for mapping flood extent have been developed by the German Aerospace Centre (DLR), the Luxembourg Institute of Science and Technology (LIST), and the Vienna University of Technology (TU Wien). Each algorithm employs distinct strategies and data inputs to address the complex scattering mechanisms, resulting in outputs that are not directly comparable at first glance (see Table 1). The single-image algorithm from DLR estimates the total water extent captured in an image, which includes both seasonal and permanent water bodies as well as flooded areas. Next, the dual-image algorithm from LIST compares the flood image with a recent SAR scene acquired from the same orbit, analysing the statistical properties of both the backscatter intensity and the changes observed between the two SAR images. It can therefore describe recent water and flood dynamics. Finally, the time-series algorithm developed by TU Wien focuses on the difference between the flood image and a reference SAR image simulated by a harmonic backscatter model that was trained on historic Sentinel-1 observations. As a result, the TU Wien algorithm provides the flood area in relation to a long-term seasonal mean. The differences in the target variables of the three algorithms can be reconciled by using reference water maps that allow distinguishing between permanent inland water, seasonal flooding, and the real flood extent. The main scientific concepts behind each of the three algorithms are discussed in the following.

< Table 1 >

2.2.1. Single-image classifier

The algorithm from DLR is designed to derive individual scene-dependent threshold values for data of various SAR sensors acquired with different sensor configurations (i.e., polarisation, beam mode, and incidence angle) and estimates the total water extent captured in one single image. It was originally developed by Martinis et al. (2009, 2015) for automatic flood detection in TerraSAR-X/TanDEM-X data, and was adapted to Sentinel-1 data by Twele et al. (2016). The classification is initialised by an unsupervised hierarchical tile-based thresholding procedure, which solves the water detection problem even in large-size SAR data with small a priori probabilities of the class-conditional densities of water in a time-efficient manner. First, the SAR imagery are tiled according to a bi-level quadtree structure and a limited number of tiles are selected, which are characterised by a high

probability to represent a bimodal distribution of the classes to be separated (i.e., water and non-water areas). Local threshold values are computed from histograms of the selected tiles using a parametric thresholding approach (Kittler and Illingworth, 1986). A global threshold computed based on the arithmetic mean of the local thresholds is applied to the SAR data to derived an initial water mask. In order to exclude water look-alikes and to reduce under-estimations, the initial classification result is optimised using a fuzzy logic-based post-classification approach by combining different information sources (backscatter, elevation and slope information as well as size of initially derived water bodies). Fuzzy region growing is performed in order to iteratively enlarge the water bodies until a tolerance criterion is reached and to increase the spatial homogeneity of the detected water areas. The HAND index is used to reduce potential misclassification in non-flood-prone regions with an empirically defined value above the drainage network. Finally, the monthly reference water reference maps are used to separate flooded areas from permanent or seasonal water bodies.

2.2.2. Dual-image classifier

LIST's flood mapping algorithm is fundamentally based on a dual-image approach utilising SAR from the same orbit, applying a sequence of statistical backscatter modelling, region growing and change detection (Matgen et al., 2011). It was initially designed to enable an automated on-demand mapping of water bodies to support disaster risk reduction at large scale. It later evolved into an always-on systematic monitoring tool that analyses newly obtained pairs of SAR images acquired from the same orbit and updates a regional floodwater extent with each new image acquisition (Chini et al., 2017, 2020). This algorithm operates iteratively, enforcing a systematic mapping of water body and flood dynamics on a large scale. The process is initiated by calibrating the parameters of the probability density functions (PDFs) to automatically and adaptively retrieve thresholds for the region-growing process. This involves modelling backscatter values linked to open water bodies and changes derived from flood and difference images, respectively. The employed hierarchical split-based approach identifies specific subsets of the images characterised by a substantial amount of water and changed pixels, where the bimodality of the histogram becomes evident. This characteristic facilitates a more robust estimation of the model parameters. The advantages of this dual-image method include its ability to distinguish between floodwater and pre-flood water bodies while simultaneously lever-

aging the fact that image pairs allow distinguishing slow and fast changing processes impacting backscatter. This allows filtering out categories that exhibit water-like backscattering values, including shadows and smooth surfaces, as well as improving the detection of backscatter reduction caused by vegetation and dry soils. Utilising reference and flood images from the same relative orbit and with identical incidence angles minimises false alarms resulting from varying geometrical acquisition characteristics. Furthermore, selecting images that are temporally closest reduces the effects of variations in vegetated regions (Zhao et al., 2021b), rendering this method particularly effective for Sentinel-1 data, which features a 6-day repeat cycle and ensures systematic and consistent image collection. This change detection configuration allows for the identification of waters that have emerged since the previous satellite acquisition. Subsequently, the algorithm analyses regions where the floodwater might have diminished in comparison to the reference image. The two types of detected changes are ultimately employed to update the flood extent map generated in the previous satellite cycle.

2.2.3. Time-series classifier

The time-series based flood mapping algorithm is based on two decades of research carried out at TU Wien aimed at large-scale monitoring of surface water dynamics from SAR data. Initial research concentrated on monitoring wetlands in boreal and sub-arctic environments, where simple thresholding methods proved effective due to the strong contrast between water bodies and surrounding land areas (Bartsch et al., 2007). However, when applying these methods to regions in Africa (Bartsch et al., 2009) and Asia (Greifeneder et al., 2014), it became clear that more sophisticated approaches were necessary to account for spatial backscatter patterns. This realisation led Schlaffer et al. (2015, 2016) to develop a harmonic backscatter model that, after calibration with historical backscatter time series, enables the simulation of expected backscatter values for each pixel and day of the year. By comparing observed backscatter with expected values, it becomes possible to identify anomalously low or high backscatter, with low values indicating open flood water and high values pointing to flooded vegetation. To quantify the uncertainty, the difference between observed and expected backscatter was interpreted as a measure of confidence, prompting the introduction of PDFs for land and open water surfaces, and the estimation of flood probabilities using Bayes' theorem. While Schlaffer et al. (2017) worked with Advanced Synthetic Aperture Radar (ASAR) data from the ENVISAT mission, which

sampled backscatter observations quite uniformly over the entire incidence angle range, the application of this method to Sentinel-1 data proved challenging due to the mission's systematic coverage, which results in very uneven data sampling at different locations on the Earth. Therefore, Bauer-Marschallinger et al. (2022) had to adopt the Bayesian inference model for application with Sentinel-1 IW data collected from different ascending and descending orbits. They also refined the methods for the masking of radar shadow areas, water look-alike areas, areas of no-sensitivity due to obstructive land cover, and ill-posed SAR settings, thereby enhancing classification robustness.

2.2.4. Ensemble algorithms

The GFM ensemble algorithms integrate the results from the three individual flood mapping algorithms in order to produce two output layers, namely a binary flood map and a flood likelihood layer (Fig. 3). The binary flood map is the main GFM output and is based on the idea of combining the three flood maps by means of a majority voting mechanism. However, there are instances when only one or two of the three individual flood mapping algorithms produce valid output files for an incoming Sentinel-1 scene. Therefore, in order to make best use of all acquired scenes, the ensemble algorithm producing the binary flood maps is essentially a decision tree that considers several cases. In the standard case, when all three flood mapping algorithms yield valid results, the binary flood map is generated by classifying pixels as flooded when at least two of the three algorithms had classified the pixels as flooded. In cases where one algorithm fails to provide a result, the remaining two algorithms ideally reach a consensus. If there is disagreement between them, the classification with the greater confidence level is selected. If both algorithms disagree but have equal confidence, the ensemble defaults to classifying the pixel as flooded. If only a single algorithm returns a result, this result is adopted by the ensemble.

< Fig. 3 >

To ensure that known water bodies are not mistakenly marked as flooded areas, all results are corrected using the monthly reference water maps, which include permanent and seasonal water extents (Section 2.3.1). If the majority of algorithms classify a pixel as water but it overlaps with a (semi-)permanent water body in the reference water map, this flood detection is overwritten.

The total water extent can then by determined by blending the flood extent and the reference water maps. In addition, an exclusion mask as described in Section 2.3.2 is applied to remove misclassified flood pixels arising from non-sensitivity, radar shadow, permanent low backscatter, or topographic distortions. Finally, ocean areas are excluded based on the Copernicus Water Body Mask.

The second output from the GFM ensemble module, the flood likelihood layer, is derived independently from the binary flood layer by fusing the flood likelihoods estimates from the three individual algorithms (Krullikowski et al., 2023). The flood likelihood indicates the probability of flood detection for each pixel. Lower likelihood scores signify greater confidence in non-flood classifications, while higher values indicate increasing confidence in flood classifications. Since the TU Wien's Bayesian algorithm outputs uncertainties, these are inverted to align with the likelihood values of the DLR and LIST algorithms before combining them in the ensemble. The ensemble flood likelihood is then computed as the arithmetic mean of all successfully computed likelihood layers from the three individual algorithms. While not carried out by the GFM service itself, the flood likelihood layer may be turned quite easily into a binary flood map adapted to local conditions by fine-tuning a threshold above which a pixel is classified as flood and below as non-flood.

2.3. Contextual information

Contextual information on local conditions and how they impact the SAR measurements is crucial for the correct interpretation of SAR-based flood maps, allowing users to assess the usability of the flood product and the impact of the flood. The first important contextual data layers are reference water maps that allow distinguishing between flooded areas and the 'normal' permanent and seasonal water extent as seen by the SAR sensors. To achieve this, the reference water maps must also be derived from the same SAR sensor. Failing to do so, such as when comparing SAR-derived flood maps with optical surface water data, leads to systematic differences related to the different physical sensitivities of the sensors. Furthermore, emergency managers and other users must be aware of the areas where the SAR sensor cannot detect floods due to physical factors. Unfortunately, explicit information about exclusion areas is often missing in operational services and scientific studies (Lahsaini et al., 2024; Al-Ruzouq et al., 2024). Furthermore, users must

be informed about environmental and meteorological conditions that could interfere with flood detection.

The following subsections describe the methods used by the GFM service to generate monthly reference water maps, an exclusion mask, and advisory flags, which are all tailored to the physical characteristics of the Sentinel-1 VV data. Finally, to help GFM users quickly evaluate potential flood impacts, the flood maps are combined with land cover and population datasets.

2.3.1. Reference water extent

In satellite-based flood mapping, inundation extent is typically derived by comparing crisis data with water extent under normal hydrologic conditions, either through change detection or by using static reference water masks. Change detection often involves manually (O'Grady et al., 2011; Ban and Yousif, 2012) or automatically (Hostache et al., 2012; Li et al., 2018b) selecting pre-event images from the same season. Reference water maps, derived from independent sources, can also differentiate flood waters from normal conditions (Martinis et al., 2015; Twele et al., 2016), though their suitability depends not only on matching sensor characteristics but also stable hydrologic conditions. For areas with seasonal changes, month-by-month mapping is preferable to capture temporal variations in surface water extent (Martinis et al., 2022). In this context, statistical computations on remote sensing time-series data are promising to reflect seasonality in the products (Fichtner et al., 2023). Water frequency approaches rely on calculating the frequency of water presence over time to distinguish permanent water bodies from seasonal ones (Wieland and Martinis, 2019). Median image approaches, in contrast, use the median pixel values over a reference time period to generate a single, stable representation of water extent that smoothens out transient changes, making it well-suited for identifying consistent water features.

As recommended by Martinis et al. (2022), the GFM service has derived twelve monthly reference water maps, each reflecting the extent of both permanent and seasonal water bodies. These reference water maps were produced using an ensemble water mapping algorithm based on Sentinel-1 median backscatter intensity data over a predefined time period of several years. The first version of the data was based upon two years (2019-2020), the most recent one upon five years (2017-2021). The ensemble method uses only the DLR and LIST algorithms that map water extent and calculate likelihoods for each pixel. The TU Wien algorithm was not used as it maps only flood areas. In cases where the DLR and LIST algorithms disagree on water clas-

sification, the one with the higher confidence level dictates the final result. In a post-processing step, an exclusion layer, based on a buffered version of the maximum extent of the Landsat-based Global Surface Water (GSW) product (Pekel et al., 2016) and the Copernicus DEM Water Body Mask (Franks and Rengarajan, 2023), is applied to address potential misclassification caused by radar shadows or rough surfaces. Fig. 4 shows an example of the GFM reference water maps for Bangladesh with strong hydrological variability throughout the year.

< Fig. 4 >

2.3.2. Exclusion mask

Even though it may not be apparent from visual inspection, a SAR image typically contains many pixels where flood mapping is impossible due to land cover and topography (Boni et al., 2016; Zhao et al., 2021a). For example, over dense vegetation and urban areas C-band backscatter is normally quite stable, making the SAR measurements insensitive to surface inundation. Moreover, water-lookalike areas (e.g., flat and impervious surfaces, sandy surfaces) and radar distortion areas (e.g., layover and shadow) pose challenges. For identifying affected pixels, a variety of methods and ancillary datasets have been developed. Urban areas and dense vegetation can be masked using existing land use maps and lidar-derived digital surface models (Mason et al., 2018; Grimaldi et al., 2020). Sandy areas, which often mimic water surfaces in SAR imagery, can be excluded using a sand exclusion layer derived from SAR time series (Martinis et al., 2018). Additionally, geometric and radiometric distortions in SAR images caused by topography can be filtered using the HAND index (Huang et al., 2017) and DEM-based shadow and layover masks (Mason et al., 2018). For the systematic mapping of all these effects at large scales, Zhao et al. (2021a) introduced a decision-tree-based approach for generating exclusion maps solely from SAR data. Similarly, the GFM service derived a global exclusion mask based on a statistical analysis of the Sentinel-1 datacube, refined using various ancillary data sets. This exclusion mask is an overlay of several thematic sub-masks, each designed to address specific effects:

1. *No-sensitivity areas*: Pixels, where SAR backscatter is largely insensitive to flooding, are identified using the Sentinel-1 Global Backscatter Model developed by Bauer-Marschallinger et al. (2021), a Global Forest

Change dataset for vegetation (Hansen et al., 2013), as well as static masks for urban regions (Marconcini et al., 2020).

2. *Non-water low-backscatter areas*: Tarmac, sand, and other smooth surfaces often display consistently low backscatter values, similar to those of open water surfaces. Since it is not feasible to differentiate these surface types from water surfaces based solely on their backscatter characteristics, all pixels showing low backscatter (below -15 dB) in more than 70% of the time series and not belonging to the reference water layer are masked.
3. *Topographic distortions*: Topography can distort the geometric and radiometric properties of SAR images. Taking benefit of the fact that floods are unlikely on high elevations above the nearest drainage, areas with HAND values greater than 15m are excluded (Chow et al., 2016).
4. *Sentinel-1 radar shadows*: Shadows caused by terrain (e.g., rough terrain or forest edges) and non-terrain factors are masked by comparing temporal mean backscatter values between ascending and descending Sentinel-1 tracks.
5. *Insufficient coverage*: Areas with no or insufficient historic Sentinel-1 coverage are excluded, as in these areas no parametrisation of the algorithms is possible.

The obtained binary GFM exclusion mask integrates all pixel locations where the SAR data cannot deliver the necessary information for robust flood delineation.

2.3.3. Advisory flags

While the GFM exclusion masks deal with static effects at high resolution, there are many highly dynamic phenomena that can impair the detection of flooded areas in SAR images over larger areas. In particular, the intermittent or semi-permanent occurrence of phenomena such as wet snow, frost and dry soil or wind-roughened water can result in limited flood mapping capabilities (Pulvirenti et al., 2014; Wieland and Martinis, 2019). To address this issue, the GFM service provides an advisory flag output layer, whose function is to raise the user's attention in carefully handling flood mapping results within flagged regions. In contrast to the exclusion layer, pixels highlighted by the advisory flags are not removed from the flood maps. For each incoming Sentinel-1 scene processed by the flood mapping algorithm, two distinct flags are produced in NRT:

1. *Low-regional backscatter flag*: Dry soil conditions, snow and frost can lead to a drop in backscatter, leading to wrongful flood mapping results over large areas affected by the specific weather conditions. In the GFM service those areas are outlined by comparing the monthly backscatter signature with the incoming Sentinel-1 scene at a 20 km scale. Pixels with detected low-backscatter values are then enclosed into a 14 km buffer zone, constituting the final advisory-flagged region.
2. *Rough water surface flag*: Water bodies can be affected by wind disturbances on the surface, altering significantly the typical backscatter behaviour observed by SAR. Thus, given the calm water signature from the backscatter time-series data as a reference, it becomes possible to delineate water pixels (as indicated by the reference water layer) that exhibit a significant increase in backscatter. A 5 km buffer zone around the wind-altered water pixels is flagged for potential wind impact.

Areas overlapped by both flags are highlighted separately.

2.3.4. Flood impact indicators

When complete and accurate flood maps are available it is possible to carry out rapid flood impact assessments by superimposing different exposure layers to the final flood map (Cian et al., 2024). While Sentinel-1 cannot map flooding in dense urban settings and other exclusion zones, as discussed in Section 2.3.2, the GFM service still computes two rapid flood impact indicators to address the critical need for such information during emergency situations, namely indices estimating the affected population and land cover respectively. The source of information for estimating the *affected population* is the Global Human Settlement Layer (GHSL), specifically the GHS-POP dataset (Schiavina et al., 2023). This dataset provides a raster representation of population distribution and density, indicating the number of people living within each grid cell. It is available at various spatial resolutions and for different time periods. For the GFM service, the dataset at 100 m resolution and with the Epoch 2020 of version R2022A is used. This dataset was resampled from 100 m to the 20 m grid used for the Sentinel-1 datacube (Section 2.4.1. This involved dividing the input pixels by the number of 20 m pixels that fit into one 100 m pixel. As illustrated by Fig. 5, the affected number of people is then estimated by superimposing the GFM flood layer with the resampled human population layer.

< Fig. 5 >

For obtaining a quick estimate of the *affected landcover* the GFM flood maps are superimposed upon the Global Land Cover dataset provided by the Copernicus Land Monitoring Service. The Copernicus Global Land Cover dataset includes 23 classes, is available globally at a 100 m resolution and is updated annually. This dataset was also resampled from 100 m to the 20 m grid. This information allows for an initial assessment of affected land cover or land use types, such as determining the extent of agricultural areas impacted by the flood within the observed flood extent area.

2.4. Implementation

The scientific methods outlined in the previous section were implemented within a dedicated cloud platform environment to enable its global and automatic processing in near real-time, utilising a datacube-centric processing architecture (Wagner et al., 2020). This allows for straightforward comparisons of each incoming backscatter image with the entire backscatter history, making it possible to run any type of time-series analysis on a per-pixel basis. In terms of storage and computational requirements, such a datacube solution is far more demanding than single-image SAR processing pipelines, such as the one used by Twele et al. (2016) to demonstrate the potential of Sentinel-1 IW images for fully-automatic flood mapping. However, as already pointed out by Cossu et al. in 2009, fast access to both recent and historical data requires more advanced cloud platform solutions. Since then, advancements in cloud computing technologies (Gomes et al., 2020) and datacube solutions (Chatenoux et al., 2021) have greatly enhanced capabilities for storing, processing, analysing, and disseminating large datasets like those generated by Sentinel-1. The following subsections describe the solutions adopted by the GFM service.

2.4.1. Sentinel-1 backscatter datacube

The GFM service builds upon the Sentinel-1 backscatter datacube as described by Wagner et al. (2021), which represents a complete collection of Sentinel-1 IW data for all continents (except Antarctic) sampled to a 20 m fixed-Earth grid. The datacube runs on the cloud infrastructure of the Earth Observation Data Center (EODC) (https://portal.services.eodc.eu/), enabling both near real-time image-based applications and offline analyses of multi-year time series. Like other SAR datacube solutions such as realised by the Google Earth Engine (Mullissa et al., 2021), it solves the problem of providing fast and efficient access to Sentinel-1 backscatter time se-

ries by projecting all Sentinel-1 IW images, which come as variable swath-based images, onto a fixed-Earth grid before tiling. This preprocessing step, though resource-intensive, is essential because performing on-demand Range-Doppler terrain correction is time-consuming, especially when covering large regions and/or extended time periods (Navacchi et al., 2022). A key feature of this datacube solution is the use of the Equi7Grid that employs the equidistant azimuthal projection and divides the Earth surface into seven continental zones (Bauer-Marschallinger et al., 2014). Unlike other commonly used large-area grids, the Equi7Grid minimises shape distortions even near the zone boundaries. In comparison to the Universal Transverse Mercator (UTM) based grid as used for Landsat and Sentinel-2, the Equi7Grid offers the advantages of a smaller number of zones (7 instead of 62) and reduced data redundancy (3% instead of 34%) (Bauer-Marschallinger and Falkner, 2023). Thanks to these specifications, the yearly data volume per satellite is less than 50 TB, whereas the number of pixels is approximately 379 billion. The backscatter data are stored as sigma nought (σ°) values and not as radiometrically-terrain-corrected gamma nought (γ°_{RTC}) values as proposed by Small (2011). While the latter was recognised by the Committee on Earth Observation Satellites (CEOS) as the Analysis Ready Data (ARD) format for normalised radar backscatter data, it primarily improves the classification of SAR data over undulating terrain (Dostalova et al., 2022). Its benefits are less obvious in valley bottoms and flat areas, which are most relevant for flood mapping. Therefore, for the GFM service, we will await the official switch to γ°_{RTC}, which is expected to happen in the 2026+ timeframe.

2.4.2. Near real-time workflow

The NRT data production workflow operates on a fully independent processing environment within EODC's cloud infrastructure. This setup includes 570 virtual CPUs (vCPUs) and 3 TB of memory, distributed across multiple worker units to ensure a service availability of 99%. As illustrated by Fig. 2, the NRT workflow starts from fetching the latest Sentinel-1 IW images. Only Ground Range Detected at High resolution (GRDH) images in VV polarisation are used, while VH polarisation is neglected. The incoming scenes are then preprocessed and registered in the datacube. The output of the preprocessing routine is encoded and gridded SAR data ready for both spatial and temporal analysis. The Equi7Grid with a 20 m pixel spacing and a 300km gridding (T3 level) serves as efficient working grid representation for all steps in the data processing workflow. Consequently, all input datasets,

including auxiliary datasets from external sources, must be re-projected to the Equi7Grid beforehand. After the successful preprocessing, the NRT flood data production workflow is triggered. First, the tiled backscatter as well as auxiliary data sets are mosaicked and cut to cover the whole extent of the input Sentinel-1 scene. As a next step, the processing of the individual flood mapping algorithms is initiated. For the dual-image classifier described in Section 2.2.2 the previous image acquired from the same orbit is extracted as additional input. Once the individual algorithms have been executed, their results are registered in dedicated databases and the ensemble algorithm is triggered. In the ensemble, described in 2.2.4, the observed flood extent, likelihood values, observed water extent and the exclusion mask are produced and afterwards registered. As a last step, the ensemble outputs are re-projected to the WebMercator projection which is used in the dissemination system described in Section 2.4.4.

2.4.3. Archive processing

In addition to the NRT delivery of the GFM flood products, we have created a complete GFM data archive using all available Sentinel-1 IW acquisitions from 2015 onwards, totalling approximately 2 million scenes. This offline processing was conducted in the high-performance-computing environment at the Vienna Scientific Cluster (https://vsc.ac.at/). The GFM archive is continuously expanding, with efforts focused on ensuring compatibility between the software versions used for both NRT and archive processing chains. The first version of the GFM data archive, based on GFM NRT version v2.1.0, was released end of 2023. The current version of the archive was processed with GFM NRT version v3.1.0 in early 2024, and is planned for release early 2025. Access to the GFM data is described in the next subsection. The GFM archive processing precedes a comparable effort by Misra et al. (2024) who create a 10 years-long Sentinel-1 flood data record using a Neural Network model trained with manually labelled SAR images from selected large-scale flood events.

2.4.4. Open data access

As highlighted by Mostafiz et al. (2022), flood information should be easily accessible and continuously evaluated to maximise its usefulness for both the public and professionals. Accordingly, GFM data are freely available and accessible to all stakeholders upon registration. To meet the needs of diverse users, several dissemination systems have been established (Table 2).

One way to visualise the GFM flood maps is to use the map viewers of the European Flood Awareness System (Matthews et al., 2025a) and the Global Flood Awareness System (Matthews et al., 2025b). These map viewers enable users to visualise all GFM product layers and manually download data for specific areas of interest (AOI). For more flexible downloading, including single files or time series for one or multiple GFM output layers, a set of application programming interfaces (APIs) following the Representational State Transfer (REST) standard has been implemented. This standard facilitates access to web resources using a predefined set of operations, allowing for seamless integration with virtually any programming language (Iadanza et al., 2021). For the analysis of the GFM data in Geographic Information System (GIS) environments, a web mapping service based on the GeoServer technology was established. Finally, a dedicated webportal was set up to enable users to define AOIs, display and download the available products for the AOI, and configure the notifications for any new available data. All mentioned systems provide the latest available imagery for each Sentinel-1 overpass. Moreover, users can also request the full time-series (or a subset) of all the archived data products. Considering the constantly growing volume of the generated GFM output data, concluding the whole archive as well as NRT data, easy discoverability and access in a programmatic way is vital to include GFM data into processing workflows and applications (Groth et al., 2024). That is why, additionally to the aforementioned data access methods, we have published the GFM data as an open access collection utilising Spatio-temporal Asset Catalogs (STAC). This enables users to search the whole GFM output data for regions and time ranges of interest. Filtering based on output-specific metadata such as the amount of flooded pixels is also possible. The GFM output data itself is stored in the cloud-optimised GeoTiff (COG) format in order to improve data reading efficiency and be ready for scaleable processing workflows.

< Table 2 >

3. Results

3.1. GFM data product

The fully automatic algorithms and workflows described in the previous section yield ten data layers (Table 3) that are included in the GFM data product. The main output layers are the observed flood extent and the

flood likelihood layer. Context is provided by the reference water maps, the exclusion mask, the advisory flags, and the flood impact indicators. The observed water extent is the combination of the observed flood extent and the reference water extent. These data fields are complemented by metadata inherited from the Sentinel-1 IW swath products, including the image boundaries (footprint), and the next scheduled Sentinel-1 acquisition. The latter is important for emergency managers who are awaiting updates on the flood situation.

An exemplary GFM data product is shown in Fig. 6. This scene depicts flooded areas along the river Rhine in the province of North Rhine-Westphalia, Germany, during the disastrous flooding that hit Germany and the Benelux countries in July 2021 (Tradowsky et al., 2023). As can be learned from the backscatter image shown as background of the flood map in Fig. 6e, the region is characterised by a mix of agricultural fields, forests, urban areas (including the city of Wesel in the southwestern part of the image), and several permanent water bodies. Many forest areas, such as the "Uedemer High Forest" in the western part of the image, are located in more elevated terrain. The different landscape features are well captured by the exclusion mask layers as discussed in Section 2.3.2. Most of the exclusion areas are a result of the presence of forests and urban areas (no backscatter sensitivity) and elevated terrain (high HAND index values). In this area there are few non-water low-backscatter areas, mostly situated near water bodies contained in the reference water map. Potentially these represent new water bodies or errors in the reference water map. Radar shadow areas are very small and mostly located along forest edges, as is typical outside mountainous regions. Some erroneous radar shadow areas can be observed along the river course, likely caused by river currents or ships, which can impact ascending and descending SAR acquisitions differently.

< Fig. 6 >

As can be seen by comparing Figs. 6a to 6c, the flood maps generated by the three individual algorithms agree very well. While a systematic evaluation of the differences between the three algorithms is outside the scope of this paper, we found a satisfying agreement for most of the analysed large-scale flood events. However, local differences near the borders of the flooded areas may arise, for instance, from the way in which each algorithm incorporates region-growing and filtering processes. Nevertheless, for our example, the

ensemble flood map shown in Fig. 6e closely resembles the individual maps. Of particular interest is the comparison with the flood likelihood layer displayed in Fig. 6d. As expected, high flood likelihood values correspond to areas identified as flooded in the ensemble flood map. Additionally, it is encouraging to note that in this particular case medium likelihood values are found only near the flooded areas and permanent water bodies, while further away flood likelihood values are consistently small. This suggests that the flood likelihood layers can provide a more complete picture of the flood situation, by allowing to identify even pixels that are only partially flooded or more challenging to interpret. This impression is further strengthened when checking other flood cases where the flood likelihood values often depict the river course, whereas the flood map remains patchy.

3.2. Timeliness

As the timely dissemination of flood maps is crucial for disaster response efforts, a core requirement of the GFM service is delivering GFM output data within 8 h after each Sentinel-1 SAR acquisition. In line with the technical specifications issued by the European Commission in 2020, procedures have been put in place to ensure and evaluate service quality. A set of Key Performance Indicators (KPIs) is used for quarterly monitoring of GFM product performance (Seewald et al., 2024). The first KPI measures the percentage of time the service was available to users, with a target value of $\geq 99\%$. A monitoring system keeps track of the availabilities of all user-facing components of the GFM service. For the year 2023, a value of 99.80% was reached. The second KPI tracks the percentage of products delivered within the required 8 h timeframe from actual observation of a Sentinel-1 scene to availability of the data on the user front ends. A typical timeline is illustrated in Fig. 7: The availability of new Sentinel-1 IW GRDH images is monitored by querying the Copernicus Data Space Ecosystem every 10 min. Downloading and pre-processing the data on the EODC cloud infrastructure takes less than 10 min and 35 min respectively. The time required for the three scientific algorithms and the ensemble product varies more strongly, from 15 to 60 min with an average of approximately 45 min depending on the complexity of the SAR scene. Post-processing and placing the data on the user front ends takes less than 10 min. On days when the Sentinel-1 ground segment operates nominally, the total time from sensing to dissemination is under 5 h, whereas the time from data upload on the Copernicus Data Space Ecosystem

to delivery to the users is less than 2 h. On best-case scenarios, the system achieved a timeliness from sensing to dissemination even below 90 min.

< Fig. 7 >

3.3. Coverage of flood events

A high spatio-temporal data coverage is essential for effective flood monitoring. To identify gaps in Sentinel-1 satellite observations and detection capabilities, we evaluated the data coverage by assessing the performance of the GFM service in detecting 104 global flood events over the past three years (i.e. 2022-2024). Note that during this period only Sentinel-1A was operational. The results of this analysis are summarised in Fig. 8 and Table 4; the complete list of flood events is provided in the Appendix in Table 7. The 104 events, encompassing small, medium, and large-scale floods from all continental regions (except Antarctica), were identified using the Global Disaster Alert and Coordination System (GDACS), a cooperation framework between the United Nations, the European Commission, and disaster management organizations worldwide (https://gdacs.org/). GDACS provides details such as affected regions, event duration, fatalities, and displacement figures, supporting disaster response and coordination during major emergencies.

< Fig. 8 >

< Table 4 >

As can be seen from Table 4, the GFM service detected 70.2% of the flood events (73 out of 104), for 10 events (9.6%) no Sentinel-1 were acquired, while 21 events (20.2%) were not detected, most likely due to unfavourable timing of the Sentinel-1 acquisition, with possible failures of more than one algorithm another possible factor. Fig. 8 illustrates how detection performance of Sentinel-1A varied significantly across continents: Europe, benefitting from the overall best coverage, demonstrated the highest success rate, detecting 95% of events (19 out of 20). Asia and South America followed with a 70% detection rate, although several events were missed in both regions. Africa showed a detection rate of 65%, with 7 out of 20 events undetected, while North America detected 60% of events (9 out of 15), missing 3. Oceania, with the smallest sample size of 9 events, exhibited the lowest performance, detecting 4 events, missing 3, and encountering 2 instances of unavailable Sentinel-1 observations.

A notable finding is that all undetected events and cases of unavailable Sentinel-1 observations corresponded to small- or medium-scale floods. This highlights a critical limitation of the GFM service: its reduced capability to detect smaller flood events, particularly in regions with low temporal revisit frequencies of Sentinel-1 satellites. The most crucial factor influencing how well GFM captures flood extents is the spatial coverage pattern and the actual overpass time of the satellite(s) (Wagner et al., 2024). When local overpasses coincide with flood peaks, the GFM product aligns best with the perception of affected populations and authorities, offering the most useful information. Additionally, a dense revisit frequency enables monitoring the progression of floods from onset to peak and eventual retreat. This shows that, at present, the GFM service is most valuable for large-scale flood events, such as the 2022 Pakistan floods (Roth et al., 2023). For small- to medium-scale events, however, additional satellite observations or improved revisit strategies are needed to enhance detection capabilities.

3.4. Accuracy

In addition to timeliness and coverage, the thematic accuracy is the third key criterion for evaluating the effectiveness of the GFM service. Given that the GFM service cannot exploit more information than what is contained in the Sentinel-1 VV-polarised IW imagery itself, the main question is how well do the algorithms extract the flooded areas visible in the Sentinel-1 images? Note that this is a different question from asking how well do Sentinel-1 flood maps capture the total flood extent? In the latter case, also the basic sensor limitations play a big role. Nevertheless, since these questions are closely related, also efforts targeted to deepen our understanding of the physical characteristics of C-band VV backscatter measurements and the efficacy of the various contextual layers were undertaken. At the individual algorithm level, the algorithm development teams have conducted a series of case studies to examine specific aspects of their algorithms and advanced techniques for exploiting the Sentinel-1 data (Zhao et al., 2022; Tupas et al., 2023b,a; Roth et al., 2023; Martinis et al., 2024; Tupas et al., 2024; Garg et al., 2024; Roth et al., 2025). At the GFM product level, the ensemble flood maps have been evaluated for selected flood cases (3 every quarter of a year) and systematically on a global level, as discussed in the following.

In the dedicated GFM evaluation activities, the accuracy was determined by comparing the automatically-derived GFM binary flood maps with

human-interpreted Sentinel-1 images and computing various accuracy metrics based upon the error matrix, such as the Critical Success Index (CSI) and Overall Accuracy (OA). The OA is a global measure that treats flood and non-flood cases as equally important. As the non-flood class dominates outside of flood-affected areas, the OA can be biased towards non-flood accuracies. The CSI, on the other hand, is better suited for evaluating events that occur substantially less frequently than the alternative (Wilks, 2011). In our context, the CSI is the number of correct flood pixels divided by the total number of flood pixels in either the GFM flood map or the human-interpreted reference map. Like the OA, it scales between 0 (worst possible) and 100% (best possible value). The accuracy target for the GFM service is a CSI value of greater than 70%.

As results for the current GFM version v3.2.0 are not yet available, we report here results from version v2.1.0 that was used for generating the first version of the GFM data archive (Section 2.4.3). When computing OA and CSI values for 12 selected flood events, which occurred between 2017 and 2023, Seewald et al. (2024) found consistently high OA values (>96.6%), while CSI values varied strongly, from 11.0% to 81.1%. The accuracy target was reached for 7 of the 12 events. For the systematic evaluation at global scale, a method similar to the one used for the evaluation of the GSW product of Pekel et al. (2016) was employed. Following the guidelines given by Card (1982) and Olofsson et al. (2014), a stratified random sampling approach was implemented to evaluate how accurately a particular pixel is mapped into the categories of permanent water, seasonal water, flood, or other areas. For establishing the reference data base consisting of tens of thousands of individual points, a tool was implemented that allowed trained interpreters to perform a blind validation (i.e., without prior knowledge of the mapped class) of the sample points based on the production imagery (i.e., Sentinel-1), with visual support from Sentinel-2, and various very high resolution images provided via Google and Bing Areal maps. For Sentinel-1 and Sentinel-2, pre- and post-event time series were provided to facilitate the identification of flood events. Each sample point was interpreted multiple times to assess interpretation uncertainty. The results of the global assessment are summarised in Table 5. This table shows globally-aggregated and area-weighted OA and CSI values for the three water classes: permanent water, seasonal water, and flooded areas. Whereas the OA values suggest a high accuracy for the permanent water body class, seasonal water and flooded areas reach OA values of 74.4% and 72.0%, respectively. The CSI values are lower, ranging between

43.7% for the flood class to 64.1% for the permanent water body class. To get a better understanding of the flood detection capability under various environmental conditions, the ∼55,000 sample points were assigned to global environmental zones as proposed by Metzger et al. (2013). These zones are mainly differentiated according to their temperature (growing degree-days) and aridity (from arid, xeric, dry, mesic, moist, to wet). As can be seen in Table 6, the best validation results are obtained for regions in the temperate and tropical zones, while lower accuracies are typically observed in arid environments. This is in line with expectations given the difficulties in distinguishing sand from water in SAR images. Overall, these results suggest that the accuracy target had not yet been reached for the investigated archive version. Further work is required to determine of how much the CSI values can be increased through improvements in the algorithms, or, as will be discussed in Section 4.5, whether the lower CSI values could partially be attributed to intrinsic constraints in the statistical analysis and uncertain reference data.

< Table 5 >

< Table 6 >

4. Discussion

4.1. A paradigm shift in SAR-based flood monitoring

While there are already fully-automatic global flood monitoring services based upon optical satellite data (Li et al., 2018a), the GFM service is the first of its kind in the SAR domain, benefitting from the radars' capability to observe day and night under all weather conditions. Some of the experiences made during its first three years of operation aligned with our anticipations while others were unexpected. Probably the most notable aspect is the shift in perspective, away from the scientific focus on mapping flood scenes as accurately as possible to designing the algorithms such that they perform equally well for flood and non-flood scenes. In fact, given that only a small fraction of SAR images depict flooding, the detection of false positives was the biggest concern during the initial phase of the GFM service. The main reasons for overdetection are discussed in the following subsection (Section 4.2). Since it is impossible to create an error-free scientific algorithm that entirely eliminates overdetections, this issue cannot be resolved purely through

scientific and technical methods but requires careful consideration of the way of the results are communicated to the users of the data. Another challenge is that Sentinel-1, like any other instrument, cannot detect all flooded areas due to various technical and scientific constraints. The main causes of underdetection in flood situations as encountered during the first three years of GFM operation are explored in Section 4.3. From a user perspective, one of the key limitations of the GFM service is its inability to map flooding in urban areas. In this context, the GFM exclusion mask is crucial, as it informs the users where they cannot expect to obtain information from the Sentinel-1 measurements. Equally important for the users are the suitability of the reference water maps (Section 4.4), and the question of how to interpret validation results (Section 4.5). Another pressing issue encountered during the first three years of operation has been the insufficient temporal coverage, especially during the period when only one Sentinel-1 satellite was operational. Solutions to this challenge are discussed in Section 4.6.

4.2. Overdetection in non-flood situations

Overdetection in non-flood situations occurs when dynamic land surface processes other than flooding cause backscatter to drop to low values typical for water surfaces. Figure 9 shows three common cases of overdetection encountered during the first three years of operation. Probably the most problematic case from a service point of view is overdetection in agricultural and grassland areas, as illustrated in the example of Fig. 9a. This has several causes, including signal attenuation during the early stages of crop growth (Arias et al., 2022; Reuß et al., 2024) and rapid changes in surface roughness and crop cover due to farming activities (Zhu et al., 2019). These effects are exacerbated when the soils are dry, as this reduces backscatter from fertile soils. As a result, depending on crop type and weather conditions, false positive rates can be quite high in some agricultural regions. Particularly the time-series algorithm as described by Bauer-Marschallinger et al. (2022) is impacted, given that the harmonic backscatter model − which is used to predict non-flood backscatter − cannot account for crop rotation practices. Therefore, Tupas et al. (2024) suggested replacing the harmonic backscatter model with an exponential filtering approach that better accounts for changing land surface backscatter.

< Fig. 9 >

The second, and most significant case in terms of the area affected, is the overestimation of flood areas in arid environments. While this issue is more pronounced in certain desert regions, such as northwestern Iraq, anomalies appear and disappear in many arid regions without clear spatio-temporal patterns. Due to the lack of systematic studies, the exact causes of these anomalies remain speculative. One likely reason is that many arid regions have low backscatter values, close to the threshold used to create the non-water low-backscatter exclusion layer. As a result, even minor changes in land surface conditions or speckle can cause pixels to be mistakenly classified as flooded. Potential natural causes for changes in backscatter include the movement of sand (Abdelkareem et al., 2020), which seems to be the primary factor contributing to the false positives shown in Fig. 9b, erosion and deposition processes triggered by rainfall, and variations in soil moisture levels. The effect of soil moisture on backscatter can vary; it may increase or decrease depending on the presence of subsurface scatterers (Wagner et al., 2022).

The third case of overdetection occurs when the land surface freezes or gets covered by snow and ice, which can cause a significant drop in backscatter (Nagler and Rott, 2000; Park et al., 2011; Pulvirenti et al., 2014). When this happens over larger areas, it is often well captured by GFM's low-regional-backscatter advisory flag. However, when temperatures fluctuate around 0°C, there may be considerable spatial variability in the Sentinel-1 images, with small patches of low backscatter caused by either frost, ice, wet snow, or flooding. In this case it is impossible to decide where the GFM flood map is correct or where not. An example is a flood that affected large areas in northwestern Europe in early January 2024 (see Fig. 9c). As temperatures started to drop below 0°C in the Netherlands, flooded meadows and agricultural fields began to freeze, likely leading to scattered patches of overestimation.

For all the cases discussed above, further research is needed to gain a deeper understanding of the physical mechanisms behind false alarms and to develop methods for correcting - or at least improving the flagging of these effects. As mentioned earlier, the low-regional-backscatter advisory flag generally performs well in identifying potential issues caused by snow or frost. However, flagging changes in already dry areas, such as deserts, remains a challenge. Additionally, advisory flags are typically not raised for overdetection in agricultural areas, as the impact of this phenomenon is usually confined to smaller areas than in the case of frost or drought.

4.3. Underdetection in flood situations

Ironically, the concern over overdetection errors in non-flood situations initially led to underdetection errors in flood situations. In an attempt to reduce "noise" (e.g. speckle, isolated pixels) in the GFM flood maps, refining post-processing and merging strategies were implemented that effectively act as low-pass filters. While this helped mitigating the impact of speckle and small-scale land cover effects, they inadvertently hampered the capability to detect small-scale and spatially scattered flood areas (Roth et al., 2025). This problem will be partly solved by an update of the post-processing algorithms planned for 2025. Nonetheless, more research will be needed to balance overestimation errors in non-flood cases and underestimation of actual flood areas. This challenge is not unique to the GFM service but is a broader issue within the field of SAR-based flood mapping. To date, many studies are limited to selected datasets coinciding with flood events, while disregarding the much more common non-flood situations. In contrast, the GFM service − to fulfil its monitoring mission − processes per day hundreds of individual data takes to flood products. Naturally, most of these products do not cover any flood and may be exposed to overestimation.

Another important aspect that needs to be balanced is the size of the exclusion areas and the magnitude of underdetection errors, which are, by definition, only assessed in the non-excluded areas. Expanding the exclusion areas to include more challenging zones could help minimise underdetection errors, thereby improving validation results. However, this would come at the cost of reducing the spatial coverage of the GFM service. Conversely, reducing the size of the exclusion mask would increase coverage but may lead to larger classification errors. Although the current GFM exclusion mask may seem extensive at first glance, it's important to consider that, due to topography, only a relatively small portion of land is prone to flooding, mostly following valleys and plains. Additionally, in some parts of the world, large portions of the land are covered by forests, sand, or other land cover types that hinder flood mapping. Considering this, the GFM exclusion mask looks plausible, striking a reasonable balance between maximising coverage and minimising underdetection errors. Nonetheless, it is evident that expanding the coverage would be beneficial, potentially through the use of additional data, improved algorithms, or a combination of both.

From a technical perspective, the data set that would be the easiest to add to the GFM workflow is the VH polarisation also acquired by the Sentinel-1 IW mode. As noted before, this second image channel is currently discarded

due to cost reasons. As already discussed by Boni et al. (2016) and Roth et al. (2025), this can lead to an underestimation in the presence of certain types of vegetation and wind. For the vegetation case, Fig. 10 illustrates the comparison between VV and VH images for a flood along the river Shire in Malawi in January 2022. The VH image detects more flooded areas than the VV image, particularly along the tributary rivers Lukhubula and Mwamphanzi, which flow into the Shire from the western hills. January falls in the middle of the rainy season in Malawi, so grasses and agricultural crops were tall when the flood occurred. The better detection of flooded areas by VH, compared to VV, is likely due to the double-bounce effect created by floodwater beneath the grasses or crops, which can increase backscatter and obscure flood detection. The VV polarisation is particularly sensitive to this effect, while VH remains less affected. Therefore, incorporating VH polarisation can provide a more complete flood map for tall grass and crop canopies. This is also true for windy conditions, where VV backscatter from wind-roughened water surfaces is often more strongly enhanced than VH backscatter (Roth et al., 2025). However, over low-vegetated surfaces and water bodies, VH images are characterised by lower backscatter that is associated with reduced contrast and elevated noise. As this leads to higher classification errors, care must be taken that algorithms, which use both polarisations, are designed to extract the additional flood areas from VH data while avoiding higher false positive rates.

< Fig. 10 >

A second promising SAR-based dataset for flood mapping is the interferometric coherence, which is calculated by comparing the amplitude and phase information of two or more single look complex (SLC) SAR images. High coherence indicates stable scatterers, while low coherence signifies a loss of correlation in amplitude and/or phase. Since flooding causes a loss of correlation, coherence can potentially enhance flood detection in areas where it is generally high (Chini et al., 2019). Because this is the case for urban areas and arid environments, the interferometric coherence holds particular promise for these two cases. The urban case was addressed by a recent review by Zhao et al. (2025) who concluded that the coherence − and even the interferometric phase − are critical for improving flood detection in urban areas. Similarly, Garg et al. (2024) highlighted the importance of the interferometric coherence in arid regions, where floodwaters reduce coherence, while non-flooded areas exhibit stable and consistent coherence over

time. However, other factors, such as varying soil moisture conditions, can also lead to a loss of correlation. Therefore, further research is required to better understand the environmental conditions under which interferometric coherence can reliably indicate flooded areas.

4.4. Suitability of reference water maps

The suitability of the monthly reference water maps depends on their ability to match the level of detail as provided by Sentinel-1 and to reflect accurately the normal water extent for the same season. Unfortunately, these requirements could not have been fulfilled by using existing global surface water data sets. For example, relying on static water products such as the SRTM Water Body Data (NASA JPL, 2013) or the Copernicus DEM Water Body Mask (Franks and Rengarajan, 2023) would lead to an overestimation of flood extent particularly in hydrologically dynamic regions like monsoon-affected Bangladesh (Fig. 4). Martinis et al. (2022) confirm this effect through comparing different water mask products. They stress that only few studies explicitly address seasonality, and that not all seasonal water products are useful for flood mapping. The latter point is also true for the widely used Landsat-based GSW data set from Pekel et al. (2016). This data set contains a "Monthly History" product (Pekel et al., 2016) that offers intra-annual water extent through monthly layers from the past 32 years, but is sensitive to single-image artifacts such as extreme events or cloud cover. Such artifacts are removed in the GSW "Monthly Recurrence" product, which provides monthly water coverage but is averaged over a long period, thus not reflecting river dynamics or climate shifts. Last but not least, it needs to be remembered that water maps derived from optical and topographic data do not capture the same water areas as observed by Sentinel-1, which would lead to systematic errors in the Sentinel-1 flood maps.

For these reasons, a dedicated effort was needed to produce 20 m reference water maps directly from the Sentinel-1 datacube, meaning that the GFM service has delivered a completely new global high-resolution surface water data set almost as a by-product. As our global evaluation has shown (Section 3.4), the quality of the GFM reference water maps appears to be quite good, with overall accuracies of 95.6% for the permanent water extent and 74.4% for the seasonal water bodies respectively. Nonetheless, it needs to be remembered that these water extent maps only show water surfaces as sensed by Sentinel-1. More complete water maps could be derived by adopting multi-sensor approaches that combine the Sentinel-1 data with

multi-spectral optical data from Landsat or Sentinel-2 (Martinis et al., 2022) or novel bi-static measurements such as provided by Global Navigation Satellite Systems Reflectometry (GNSS-R) missions (Carreno-Luengo et al., 2024) or swath-based altimetry missions (Morrow et al., 2018).

An open question for flood mapping is the optimal length of the time series used to compute the reference water maps. Following Martinis et al. (2022), GFM uses time series of a few years from the recent past. Whereas the first versions of the reference water maps was based upon two years (2019-2020), the most recent on five years (2017-2021). While the longer time series helped to reduce misclassification and mitigate the impact of extreme events, longer aggregation periods may blur dynamic hydrological features, such as braided rivers and water reservoirs. Hence, some water surfaces that should be part of the reference water maps are wrongly shown as flooded (e.g. water reservoirs that are being filled up). An interesting special case is flooded fields used for growing rice and other semiaquatic crops. These fields are sometimes included in the reference water maps and sometimes in the flood maps. As this is confusing for the GFM users, a dedicated effort for mapping these fields based upon their pronounced seasonal backscatter behaviour, as for example done by Nguyen and Wagner (2017) over European rice fields, might be useful.

4.5. Adequacy of accuracy metrics

The results of the validation activities, as discussed in Section 3.4, have been quite mixed so far. While the results are generally satisfying, the CSI values computed for individual flood events and the global evaluation of the first version of the flood data archive (GFM v2.1.0) fall short of the GFM service's accuracy target. Insights gained from the different validation activities have already been very instructive, driving step-by-step improvements in the algorithms and workflows with each new GFM version. For example, over- and underdection errors as discussed above have already been reduced, leading to subsequent improvements in CSI values. Nonetheless, we note that in some cases the CSI and other accuracy metrics remain relatively low, even when the flood maps appear visually satisfactory (Roth et al., 2023, 2025). This raises questions regarding the adequacy of the accuracy metrics. One key issue is the lack of independent data to serve as objective ground truth for assessing how well the algorithm extracts flooded areas from Sentinel-1 images. As a result, expert-interpreted Sentinel-1 flood data are used to create flood reference datasets. However, this introduces uncertainties, which

likely lower the CSI and other accuracy metrics to an extent that remains unclear. The second issue is that, so far, the quality of flood maps has been assessed with methods as used for assessing static land cover. While critical aspects such as sampling design, response design, and analysis design are well understood for the latter (Stehman and Czaplewski, 1998; Congalton and Green, 2019), the high spatiotemporal variability of the sensitivity of the sensor to the target variable and the highly dynamic nature of floods make the evaluation of flood data much more challenging. As a result, flood mapping studies had to cope with inadequacies of metrics derived from the error matrix. For example, Landuyt et al. (2019) showed that the CSI has a bias towards large-scale floods and assigns a higher accuracy in case of overdetection in comparison to underdetection. When using the whole map for the metric computation, the agreement between the reference and classification will generally be much larger compared to their difference. Further, the expected autocorrelation of neighbouring pixels in satellite observations leads to many redundant pixels being validated. Consequently, Landwehr et al. (2024) suggested the definition of an appropriate sampling design for computing the metrics and choosing an adequate metric for the corresponding design.

In line with our methodological approach, which views flood mapping as a geophysical variable retrieval problem rather than a classification task (Section 2.1), we believe that also the validation of flood extent data should be approached from a broader geophysical perspective. First, validation activities should clearly define their scope. Is the aim to evaluate the combined effect of sensor and retrieval algorithm on the quality of the flood extent data, or just one of these aspects? In all cases, data producers should provide estimates of the retrieval uncertainty and clearly identify exclusion areas where the sensor is insensitive to the target variable. Additionally, validation should not be limited to flood images but should also include non-flood cases (Tupas et al., 2024). It is likely that most existing algorithms are optimised for flood detection, which may limit their applicability to other regions or time periods. Moreover, methods must be developed to assess the impact of imperfect reference data on accuracy metrics. All these topics require a community effort to develop best practice guidelines, which, as already noted by Landwehr et al. (2024), are still missing. These efforts could be organised as part of the Land Product Validation subgroup of the Committee on Earth Observation Satellites (https://lpvs.gsfc.nasa.gov/).

4.6. Temporal coverage

Despite the fact that the Sentinel-1 mission provides better global coverage than any other single SAR satellite or SAR satellite constellation, our analysis presented in Section 3.3 illustrates that smaller flood events may be missed, particularly in less well-covered areas of the world. Increasing the temporal resolution of SAR acquisitions would significantly improve the ability to capture the high dynamics of floods, ensuring that flood peaks and progressions are adequately monitored. Through improvements in swath width and duty cycle, the situation will become better for the Sentinel-1 Next Generation (Torres et al., 2024). Nonetheless, substantial improvements in the GFM coverage can only be achieved by integrating further satellites into the service. The most logical candidates are other SAR missions that match the global and systematic monitoring capabilities of Sentinel-1. In this regard, two L-band SAR missions stand out, namely the NASA-ISRO Synthetic Aperture Radar (NISAR) satellite (Rosen and Kumar, 2021), which is ready for launch in early 2025, and the Radar Observing System for Europe at L-band (ROSE-L) two-satellites constellation mission (Davidson and Furnell, 2021), planned for launch in the 2028+ timeframe. ROSE-L belongs to the Copernicus programme, and its two satellites will be operated in synergy with the two Sentinel-1 satellites, with the orbit phasing yet to be determined. One option is to fly the ROSE-L satellites in convoy with the Sentinel-1 satellites, acquiring matching dual-frequency SAR imagery just minutes apart. The alternative is to phase the orbits of the four satellites to maximise daily global coverage. As we already highlighted in Wagner et al. (2024), the second option is clearly preferred by the GFM service. While dual-frequency retrievals can be expected to improve the accuracy of the flood maps to some extent (Refice et al., 2020), the more critical issue is whether the satellites can effectively capture flood dynamics, especially near the flood peak. Irrespective of the choice for the orbit phasing, research will be needed to optimally exploit the availability of interleaved C- and L-band backscatter time series.

5. Conclusions

The GFM service constitutes a significant advancement in the field of satellite-based flood monitoring. Launched in 2021 as part of the CEMS, the GFM service has demonstrated its capability to deliver flood maps with high accuracy and reliability in near real-time. When the Sentinel-1 ground

segment operates normally, the service achieves a rapid turnaround of under five hours, which is essential for timely disaster response. The flood maps are produced using an innovative ensemble approach that integrates three complementary flood mapping algorithms. These algorithms combine single-image, dual-image, and time-series techniques to improve the robustness and accuracy of the automatic flood detection. In addition to the binary flood map, a novel flood likelihood layer is generated, which often offers a more comprehensive view of the flood situation. For example, it can depict river courses more effectively than the binary flood maps. Users with their on-site knowledge can create a binary flood map that is better suited to local conditions by fine-tuning a threshold, above which a pixel is classified as flooded and below which it is classified as non-flooded.

The scientific algorithms were implemented within a cloud platform environment, leveraging a datacube-centric processing architecture. This approach is crucial for framing the flood mapping problem as a geophysical variable retrieval task, rather than a traditional image classification problem. A global 20 m Sentinel-1 datacube allows to compare each incoming backscatter image with the entire historical backscatter dataset, facilitating time-series analysis on a per-pixel basis. This setup has enabled the generation of monthly reference water maps, which differentiate flooded areas from permanent and seasonal water bodies, as well as an exclusion mask that informs users where Sentinel-1 cannot effectively map flooded areas. Advisory flags raise attention in case of ambiguous radar signals stemming from meteorologic or geomorphologic circumstances, and flood impact indicators give quick insight into affected population and land cover. Additionally, the datacube has enabled the creation of a global flood data archive spanning the entire Sentinel-1 mission from 2015 onwards. The GFM flood archive is continuously updated with NRT data, while regular reprocessing efforts are conducted to ensure compatibility between the NRT and archive data.

Despite its successes, the GFM service faces several scientific and technical challenges. One of the primary issues is the reduction of false positives, especially in agricultural and arid regions, as well as in areas with frozen or snow-covered land surfaces. These false positives arise from the complex scattering mechanisms as depicted by SAR imagery, which are influenced by a range of environmental factors, including soil moisture and vegetation dynamics. Another significant challenge is the underdetection of floods in certain conditions. The reliance on VV polarisation alone, without considering VH polarisation, can lead to underestimation in areas with dense vegetation

or rough water surfaces. Additionally, urban areas pose difficulties for flood detection due to the complex interaction of microwaves with building structures. Preliminary validation results as reported in this paper showed that algorithmic improvements are still needed, several of which are in the process of being implemented and tested. Moreover, work is needed to advance validation practices, approaching the problem from a broader geophysical perspective and accounting for uncertainties in the flood reference data. For the users, another pressing issue is that particularly smaller flood events go undetected due to insufficient data coverage. The analysis of 104 global flood events from 2022 to 2024 revealed that the GFM service, relying on only one Sentinel-1 satellite during this period, detected 70.2% of these events. However, the detection performance varied significantly across continents, with Europe demonstrating the highest success rate and Oceania the lowest. The reduced capability to detect smaller flood events, particularly in regions with low temporal revisit frequencies of Sentinel-1 satellites, highlights the need for improved data coverage.

To enhance the GFM service, several future directions are proposed. First, the integration of VH polarisation data could improve flood detection in vegetated and urban areas. Additionally, the development of more sophisticated algorithms that account for the complex scattering mechanisms in SAR imagery is essential. For instance, the consideration of double bounce signals and interferometric coherence may improve food mapping in urban areas and dense vegetation (Mason et al., 2014; Chini et al., 2019). Flood maps may be refined by improved use of ancillary data such as topographic indices and land cover (Tupas et al., 2023a). Machine learning is expected to be useful for a better modelling of overdetection cases (Misra et al., 2024). The GFM service should also continue to refine and update its exclusion mask and reference water maps, making sure that these data layers reflect changing land cover and water body dynamics. After the premature loss of Sentinel-1B, the expansion of the Sentinel-1 constellation with Sentinel-1C and the upcoming Sentinel-1D satellite is essential to maintain the performance of the service. Additionally, adopting a multi-sensor approach, which includes data from other satellite missions such as ROSE-L, would significantly improve the ability to capture flood dynamics and reduce over- and underdetection. The aim is to gather enough satellite imagery to monitor the progression of floods from onset to peak and retreat with improved thematic accuracy. Although not covered in this review, the integration of the GFM flood maps with topographic data and hydraulic models to provide

more complete flood extent maps and flood depth estimates holds significant potential.

The Sentinel-1-based Global Flood Monitoring service has made significant strides in operational satellite-based flood monitoring, providing timely and accurate flood maps to support disaster response efforts. While challenges remain, ongoing research and development efforts are poised to enhance the service's capabilities, ensuring it meets the evolving needs of users worldwide. By leveraging advancements in SAR technology and integrating data from multiple satellite missions, the GFM service is well set to continue to play a leading role in global flood risk management and mitigation.

CRediT authorship contribution statement

Conceptualization: Wagner, Matgen, Martinis, McCormick, Salamon; Writing – original draft: Wagner; Writing – review and editing: All authors; Formal analysis: All authors; Data curation: Stachl, Reimer, Bauer-Marschallinger, Roth, Festa, Hassaan, Chini, Li, Wieland, Kraft, Seewald, Riffler, Tupas, Zhao; Software: Stachl, Reimer, Bauer-Marschallinger, Roth, Festa, Hassaan, Chini, Li, Wieland, Kraft, Seewald, Riffler, Tupas, Zhao; Visualization: Bauer-Marschallinger, Festa, Wagner, Roth, Hassaan, Stachl, Reimer, Wieland; Validation: Seewald, Riffler; Funding acquisition: Briese, Kidd, Wagner, Bauer-Marschallinger, Matgen, Chini, Martinis, Molini; Project administration: Kidd, Briese.

Declaration of competing interest

The authors declare that they have no known competing financial interests or personal relationships that could have appeared to influence this scientific review.

Data availability

The Sentinel-1 flood data generated by the CEMS GFM service are free and open. They can be accessed as described in Section 2.4.4.

Acknowledgements

The CEMS GFM service is funded by the European Commission through the framework contract 939866-IPR-2020. TU Wien acknowledges co-funding by the Austrian Research Promotion Agency (FFG) through the ScaleFloodS

project (FO999900598).

Declaration of generative AI in scientific writing

During the preparation of this work the first author (Wolfgang Wagner) used ChatGTP and Writefull in order to improve the readability and language of the manuscript. After using these tools, he and all co-authors reviewed and edited the content as needed and take full responsibility for the content of the published article.

Appendix: List of flood events

The 104 flood events selected for this study were derived from the Global Disaster Alert and Coordination System (GDACS). GDACS offers real-time flood alerts and comprehensive data to aid disaster response (De Grove et al., 2007). The alerts issued by GDACS are based on information gathered from authoritative institutions, media outlets, and scientific institutions, rather than automated systems. These alerts rely on manual evaluations of the flood impacts, which are performed by the Dartmouth Flood Observatory. The assessments include various metrics such as the area affected, the duration of the flood, severity, fatalities, and the number of displaced persons. The magnitude of each event is computed according to:

$$\text{Magnitude} = \ln(\text{duration}) \times \text{severity class} \times \frac{\text{affected region}}{100}$$

where the affected region is measured in km^2, estimated from the polygon that encompasses all the place names reported in the media. For single-day events, the duration is set to 1.1 for calculation purposes. The GDACS alert score is translated into an alert level or colour as follows:

- *Large-scale floods:* GDACS score of 2.5, corresponding to a Red alert for more than 1,000 dead or 800,000 displaced.
- *Medium-scale floods:* GDACS score of 1.5, corresponding to an alert if there are more than 100 dead or 80,000 displaced.
- *Small-scale floods:* GDACS score of 0.5, corresponding to a Green alert for all other floods.

Our dataset (Table 7) contains all large- and medium-scale flood events that occurred between 2022 and 2024, ensuring comprehensive coverage of significant global floods during this period. In addition, small-scale flood events were included to obtain up to 20 flood events per continental region and test the ability of the GFM service to detect less severe events.

< Table 7 >

References

Abdelkareem, M., Gaber, A., Abdalla, F., El-Din, G.K., 2020. Use of optical and radar remote sensing satellites for identifying and monitoring active/inactive landforms in the driest desert in Saudi Arabia. Geomorphology 362, 107197. URL: https://linkinghub.elsevier.com/retrieve/pii/S0169555X20301690, doi:10.1016/j.geomorph.2020.107197.

Ajmar, A., Boccardo, P., Broglia, M., Kucera, J., Giulio-Tonolo, F., Wania, A., 2017. Response to Flood Events: The Role of Satellite-based Emergency Mapping and the Experience of the Copernicus Emergency Management Service, in: Molinari, D., Menoni, S., Ballio, F. (Eds.), Geophysical Monograph Series. 1 ed.. Wiley, pp. 211–228. URL: https://agupubs.onlinelibrary.wiley.com/doi/10.1002/9781119217930.ch14, doi:10.1002/9781119217930.ch14.

Al-Ruzouq, R., Shanableh, A., Jena, R., Gibril, M.B.A., Hammouri, N.A., Lamghari, F., 2024. Flood susceptibility mapping using a novel integration of multi-temporal sentinel-1 data and eXtreme deep learning model. Geoscience Frontiers 15, 101780. URL: https://linkinghub.elsevier.com/retrieve/pii/S1674987124000045, doi:10.1016/j.gsf.2024.101780.

Amitrano, D., Di Martino, G., Di Simone, A., Imperatore, P., 2024. Flood Detection with SAR: A Review of Techniques and Datasets. Remote Sensing 16, 656. URL: https://www.mdpi.com/2072-4292/16/4/656, doi:10.3390/rs16040656.

Arias, M., Campo-Bescos, M.A., Arregui, L.M., Gonzalez-Audicana, M., Alvarez-Mozos, J., 2022. A New Methodology for Wheat Attenuation Correction at C-Band VV-Polarized Backscatter Time Series. IEEE Transactions on Geoscience and Remote Sensing 60, 1–14. URL: https://ieeexplore.ieee.org/document/9777738/, doi:10.1109/TGRS.2022.3176144.

Ban, Y., Yousif, O.A., 2012. Multitemporal Spaceborne SAR Data for Urban Change Detection in China. IEEE Journal of Selected Topics in Applied Earth Observations and Remote Sensing 5, 1087–1094. URL: https://ieeexplore.ieee.org/document/6230616/, doi:10.1109/JSTARS.2012.2201135.

Bartsch, A., Kidd, R.A., Pathe, C., Scipal, K., Wagner, W., 2007. Satellite radar imagery for monitoring inland wetlands in boreal and sub-arctic environments. Aquatic Conservation: Marine and Freshwater Ecosystems 17, 305–317. URL: https://onlinelibrary.wiley.com/doi/10.1002/aqc.836, doi:10.1002/aqc.836.

Bartsch, A., Wagner, W., Scipal, K., Pathe, C., Sabel, D., Wolski, P., 2009. Global monitoring of wetlands – the value of ENVISAT ASAR Global mode. Journal of Environmental Management 90, 2226–2233. URL: https://linkinghub.elsevier.com/retrieve/pii/S0301479708000431, doi:10.1016/j.jenvman.2007.06.023.

Bauer-Marschallinger, B., Cao, S., Navacchi, C., Freeman, V., Reuß, F., Geudtner, D., Rommen, B., Vega, F.C., Snoeij, P., Attema, E., Reimer, C., Wagner, W., 2021. The normalised Sentinel-1 Global Backscatter Model, mapping Earth's land surface with C-band microwaves. Scientific Data 8, 277. URL: https://www.nature.com/articles/s41597-021-01059-7, doi:10.1038/s41597-021-01059-7.

Bauer-Marschallinger, B., Cao, S., Tupas, M.E., Roth, F., Navacchi, C., Melzer, T., Freeman, V., Wagner, W., 2022. Satellite-Based Flood Mapping through Bayesian Inference from a Sentinel-1 SAR Datacube. Remote Sensing 14, 3673. URL: https://www.mdpi.com/2072-4292/14/15/3673, doi:10.3390/rs14153673.

Bauer-Marschallinger, B., Falkner, K., 2023. Wasting petabytes: A survey of the Sentinel-2 UTM tiling grid and its spatial overhead. ISPRS Journal of Photogrammetry and Remote Sensing 202, 682–690. URL: https://linkinghub.elsevier.com/retrieve/pii/S0924271623001971, doi:10.1016/j.isprsjprs.2023.07.015.

Bauer-Marschallinger, B., Sabel, D., Wagner, W., 2014. Optimisation of global grids for high-resolution remote sensing data. Computers & Geosciences 72, 84–93. URL: https://www.sciencedirect.com/science/article/pii/S0098300414001629, doi:10.1016/j.cageo.2014.07.005.

Bentivoglio, R., Isufi, E., Jonkman, S.N., Taormina, R., 2022. Deep learning methods for flood mapping: a review of existing applications and future research directions. Hydrology and Earth System Sciences 26, 4345–4378. URL: https://hess.copernicus.org/articles/26/4345/2022/, doi:10.5194/hess-26-4345-2022.

Boni, G., Ferraris, L., Pulvirenti, L., Squicciarino, G., Pierdicca, N., Candela, L., Pisani, A.R., Zoffoli, S., Onori, R., Proietti, C., Pagliara, P., 2016. A Prototype System for Flood Monitoring Based on Flood Forecast Combined With COSMO-SkyMed and Sentinel-1 Data. IEEE Journal of Selected Topics in Applied Earth Observations and Remote Sens-

ing 9, 2794–2805. URL: https://ieeexplore.ieee.org/document/7399683/, doi:10.1109/JSTARS.2016.2514402.

Calvin, K., Dasgupta, D., Krinner, G., Mukherji, A., Thorne, P.W., Trisos, C., Romero, J., Aldunce, P., Barrett, K., Blanco, G., Cheung, W.W., Connors, S., Denton, F., Diongue-Niang, A., Dodman, D., Garschagen, M., Geden, O., Hayward, B., Jones, C., Jotzo, F., Krug, T., Lasco, R., Lee, Y.Y., Masson-Delmotte, V., Meinshausen, M., Mintenbeck, K., Mokssit, A., Otto, F.E., Pathak, M., Pirani, A., Poloczanska, E., Pörtner, H.O., Revi, A., Roberts, D.C., Roy, J., Ruane, A.C., Skea, J., Shukla, P.R., Slade, R., Slangen, A., Sokona, Y., Sörensson, A.A., Tignor, M., Van Vuuren, D., Wei, Y.M., Winkler, H., Zhai, P., Zommers, Z., Hourcade, J.C., Johnson, F.X., Pachauri, S., Simpson, N.P., Singh, C., Thomas, A., Totin, E., Arias, P., Bustamante, M., Elgizouli, I., Flato, G., Howden, M., Méndez-Vallejo, C., Pereira, J.J., Pichs-Madruga, R., Rose, S.K., Saheb, Y., Sánchez Rodríguez, R., Ürge Vorsatz, D., Xiao, C., Yassaa, N., Alegría, A., Armour, K., Bednar-Friedl, B., Blok, K., Cissé, G., Dentener, F., Eriksen, S., Fischer, E., Garner, G., Guivarch, C., Haasnoot, M., Hansen, G., Hauser, M., Hawkins, E., Hermans, T., Kopp, R., Leprince-Ringuet, N., Lewis, J., Ley, D., Ludden, C., Niamir, L., Nicholls, Z., Some, S., Szopa, S., Trewin, B., Van Der Wijst, K.I., Winter, G., Witting, M., Birt, A., Ha, M., Romero, J., Kim, J., Haites, E.F., Jung, Y., Stavins, R., Birt, A., Ha, M., Orendain, D.J.A., Ignon, L., Park, S., Park, Y., Reisinger, A., Cammaramo, D., Fischlin, A., Fuglestvedt, J.S., Hansen, G., Ludden, C., Masson-Delmotte, V., Matthews, J.R., Mintenbeck, K., Pirani, A., Poloczanska, E., Leprince-Ringuet, N., Péan, C., 2023. IPCC, 2023: Climate Change 2023: Synthesis Report. Contribution of Working Groups I, II and III to the Sixth Assessment Report of the Intergovernmental Panel on Climate Change [Core Writing Team, H. Lee and J. Romero (eds.)]. IPCC, Geneva, Switzerland. Technical Report. Intergovernmental Panel on Climate Change (IPCC). URL: https://www.ipcc.ch/report/ar6/syr/, doi:10.59327/IPCC/AR6-9789291691647. edition: First.

Card, D.H., 1982. Using known map category marginal frequencies to improve estimates of thematic map accuracy. Photogrammetric Engineering and Remote Sensing , 431–439.

Carincotte, C., Derrode, S., Bourennane, S., 2006. Unsupervised change detection on SAR images using fuzzy hidden Markov chains. IEEE Transactions on Geoscience and Remote Sensing 44, 432–441. URL: http://ieeexplore.ieee.org/document/1580728/, doi:10.1109/TGRS.2005.861007.

Carreno-Luengo, H., Ruf, C.S., Gleason, S., Russel, A., 2024. Detection of inland

water bodies under dense biomass by CYGNSS. Remote Sensing of Environment 301, 113896. URL: https://linkinghub.elsevier.com/retrieve/pii/S0034425723004479, doi:10.1016/j.rse.2023.113896.

Chatenoux, B., Richard, J.P., Small, D., Roeoesli, C., Wingate, V., Poussin, C., Rodila, D., Peduzzi, P., Steinmeier, C., Ginzler, C., Psomas, A., Schaepman, M.E., Giuliani, G., 2021. The Swiss data cube, analysis ready data archive using earth observations of Switzerland. Scientific Data 8, 295. URL: https://www.nature.com/articles/s41597-021-01076-6, doi:10.1038/s41597-021-01076-6.

Chini, M., Hostache, R., Giustarini, L., Matgen, P., 2017. A Hierarchical Split-Based Approach for Parametric Thresholding of SAR Images: Flood Inundation as a Test Case. IEEE Transactions on Geoscience and Remote Sensing 55, 6975–6988. URL: http://ieeexplore.ieee.org/document/8017436/, doi:10.1109/TGRS.2017.2737664.

Chini, M., Pelich, R., Hostache, R., Matgen, P., Bossung, C., Campanella, P., Rudari, R., Bally, P., 2020. Systematic and Automatic Large-Scale Flood Monitoring System Using Sentinel-1 SAR Data, in: IGARSS 2020 - 2020 IEEE International Geoscience and Remote Sensing Symposium, IEEE, Waikoloa, HI, USA. pp. 3251–3254. URL: https://ieeexplore.ieee.org/document/9323428/, doi:10.1109/IGARSS39084.2020.9323428.

Chini, M., Pelich, R., Pulvirenti, L., Pierdicca, N., Hostache, R., Matgen, P., 2019. Sentinel-1 InSAR Coherence to Detect Floodwater in Urban Areas: Houston and Hurricane Harvey as A Test Case. Remote Sensing 11, 107. URL: https://www.mdpi.com/2072-4292/11/2/107, doi:10.3390/rs11020107.

Chow, C., Twele, A., Martinis, S., 2016. An assessment of the Height Above Nearest Drainage terrain descriptor for the thematic enhancement of automatic SAR-based flood monitoring services, Edinburgh, United Kingdom. p. 999808. URL: http://proceedings.spiedigitallibrary.org/proceeding.aspx?doi=10.1117/12.2240766, doi:10.1117/12.2240766.

Cian, F., Delgado Blasco, J.M., Ivanescu, C., 2024. Improving rapid flood impact assessment: An enhanced multi-sensor approach including a new flood mapping method based on Sentinel-2 data. Journal of Environmental Management 369, 122326. URL: https://linkinghub.elsevier.com/retrieve/pii/S0301479724023120, doi:10.1016/j.jenvman.2024.122326.

Congalton, R.G., Green, K., 2019. Assessing the Accuracy of Remotely Sensed Data: Principles and Practices, Third Edition. 3 ed., CRC Press. URL: https://www.taylorfrancis.com/books/9780429629358, doi:10.1201/9780429052729.

Cossu, R., Schoepfer, E., Bally, P., Fusco, L., 2009. Near real-time SAR-based processing to support flood monitoring. Journal of Real-Time Image Processing 4, 205–218. URL: http://link.springer.com/10.1007/s11554-009-0114-4, doi:10.1007/s11554-009-0114-4.

Dasgupta, A., Grimaldi, S., Ramsankaran, R., Pauwels, V.R.N., Walker, J.P., Chini, M., Hostache, R., Matgen, P., 2018. Flood Mapping Using Synthetic Aperture Radar Sensors From Local to Global Scales, in: Schumann, G.J., Bates, P.D., Apel, H., Aronica, G.T. (Eds.), Geophysical Monograph Series. 1 ed.. Wiley, pp. 55–77. URL: https://agupubs.onlinelibrary.wiley.com/doi/10.1002/9781119217886.ch4, doi:10.1002/9781119217886.ch4.

Davidson, M.W.J., Furnell, R., 2021. ROSE-L: Copernicus L-Band Sar Mission, in: 2021 IEEE International Geoscience and Remote Sensing Symposium IGARSS, IEEE, Brussels, Belgium. pp. 872–873. URL: https://ieeexplore.ieee.org/document/9554018/, doi:10.1109/IGARSS47720.2021.9554018.

De Grove, T., Kugler, Z., Brakenridge, R., 2007. Near Real-time Flood Alerting for the Global Disaster Alert and Coordination System, in: Proceedings of ISCRAM2007, VUBPRESS Brussels University Press, Brussels, Belgium. pp. 33–40. URL: https://publications.jrc.ec.europa.eu/repository/handle/JRC40032.

De Zan, F., Monti Guarnieri, A., 2006. TOPSAR: Terrain Observation by Progressive Scans. IEEE Transactions on Geoscience and Remote Sensing 44, 2352–2360. URL: http://ieeexplore.ieee.org/document/1677745/, doi:10.1109/TGRS.2006.873853.

Denis, G., De Boissezon, H., Hosford, S., Pasco, X., Montfort, B., Ranera, F., 2016. The evolution of Earth Observation satellites in Europe and its impact on the performance of emergency response services. Acta Astronautica 127, 619–633. URL: https://linkinghub.elsevier.com/retrieve/pii/S0094576515303337, doi:10.1016/j.actaastro.2016.06.012.

DeVries, B., Huang, C., Armston, J., Huang, W., Jones, J.W., Lang, M.W., 2020. Rapid and robust monitoring of flood events using Sentinel-1 and

Landsat data on the Google Earth Engine. Remote Sensing of Environment 240, 111664. URL: https://linkinghub.elsevier.com/retrieve/pii/S003442572030033X, doi:10.1016/j.rse.2020.111664.

Dostalova, A., Navacchi, C., Greimeister-Pfeil, I., Small, D., Wagner, W., 2022. The effects of radiometric terrain flattening on SAR-based forest mapping and classification. Remote Sensing Letters 13, 855–864. URL: https://www.tandfonline.com/doi/full/10.1080/2150704X.2022.2092911, doi:10.1080/2150704X.2022.2092911.

Fichtner, F., Mandery, N., Wieland, M., Groth, S., Martinis, S., Riedlinger, T., 2023. Time-series analysis of Sentinel-1/2 data for flood detection using a discrete global grid system and seasonal decomposition. International Journal of Applied Earth Observation and Geoinformation 119, 103329. URL: https://linkinghub.elsevier.com/retrieve/pii/S1569843223001516, doi:10.1016/j.jag.2023.103329.

Franks, S., Rengarajan, R., 2023. Evaluation of Copernicus DEM and Comparison to the DEM Used for Landsat Collection-2 Processing. Remote Sensing 15, 2509. URL: https://www.mdpi.com/2072-4292/15/10/2509, doi:10.3390/rs15102509.

Garg, S., Dasgupta, A., Motagh, M., Martinis, S., Selvakumaran, S., 2024. Unlocking the full potential of Sentinel-1 for flood detection in arid regions. Remote Sensing of Environment 315, 114417. URL: https://linkinghub.elsevier.com/retrieve/pii/S0034425724004437, doi:10.1016/j.rse.2024.114417.

Giustarini, L., Hostache, R., Matgen, P., Schumann, G.J.P., Bates, P.D., Mason, D.C., 2013. A Change Detection Approach to Flood Mapping in Urban Areas Using TerraSAR-X. IEEE Transactions on Geoscience and Remote Sensing 51, 2417–2430. URL: http://ieeexplore.ieee.org/document/6297453/, doi:10.1109/TGRS.2012.2210901.

Gomes, V., Queiroz, G., Ferreira, K., 2020. An Overview of Platforms for Big Earth Observation Data Management and Analysis. Remote Sensing 12, 1253. URL: https://www.mdpi.com/2072-4292/12/8/1253, doi:10.3390/rs12081253.

Greifeneder, F., Wagner, W., Sabel, D., Naeimi, V., 2014. Suitability of SAR imagery for automatic flood mapping in the Lower Mekong Basin. International Journal of Remote Sensing 35, 2857–2874. URL: https://www.tandfonline.com/doi/full/10.1080/01431161.2014.890299, doi:10.1080/01431161.2014.890299.

Grimaldi, S., Xu, J., Li, Y., Pauwels, V., Walker, J., 2020. Flood mapping under vegetation using single SAR acquisitions. Remote Sensing of Environment 237, 111582. URL: https://linkinghub.elsevier.com/retrieve/pii/S0034425719306029, doi:10.1016/j.rse.2019.111582.

Groth, S., Wieland, M., Henkel, F., Martinis, S., 2024. Global reference water information for flood monitoring: Increasing accessibility with STAC. URL: https://meetingorganizer.copernicus.org/EGU24/EGU24-3849.html, doi:10.5194/egusphere-egu24-3849.

Hansen, M.C., Potapov, P.V., Moore, R., Hancher, M., Turubanova, S.A., Tyukavina, A., Thau, D., Stehman, S.V., Goetz, S.J., Loveland, T.R., Kommareddy, A., Egorov, A., Chini, L., Justice, C.O., Townshend, J.R.G., 2013. High-Resolution Global Maps of 21st-Century Forest Cover Change. Science 342, 850–853. URL: https://www.science.org/doi/10.1126/science.1244693, doi:10.1126/science.1244693.

Hostache, R., Matgen, P., Wagner, W., 2012. Change detection approaches for flood extent mapping: How to select the most adequate reference image from online archives? International Journal of Applied Earth Observation and Geoinformation 19, 205–213. URL: https://linkinghub.elsevier.com/retrieve/pii/S0303243412000992, doi:10.1016/j.jag.2012.05.003.

Huang, C., Nguyen, B.D., Zhang, S., Cao, S., Wagner, W., 2017. A Comparison of Terrain Indices toward Their Ability in Assisting Surface Water Mapping from Sentinel-1 Data. ISPRS International Journal of Geo-Information 6, 140. URL: http://www.mdpi.com/2220-9964/6/5/140, doi:10.3390/ijgi6050140.

Iadanza, C., Trigila, A., Starace, P., Dragoni, A., Biondo, T., Roccisano, M., 2021. IdroGEO: A Collaborative Web Mapping Application Based on REST API Services and Open Data on Landslides and Floods in Italy. ISPRS International Journal of Geo-Information 10, 89. URL: https://www.mdpi.com/2220-9964/10/2/89, doi:10.3390/ijgi10020089.

Ignatenko, V., Dogan, O., Radius, A., Nottingham, M., Muff, D., Lamentowski, L., Leprovost, P., Vehmas, R., Seilonen, T., Vilja, P., 2024. ICEYE Microsatellite SAR Constellation: SAR data quality improvements and new Dwell imaging mode, in: EUSAR 2024; 15th European Conference on Synthetic Aperture Radar, pp. 1118–1192.

Imhoff, M.L., Vermillion, C., Story, M., Choudhury, A., Gafoor, A., Polcyn, F., 1987. Monsoon Flood Boundary Delineation and Damage Assessment Using

Space Borne Imaging Radar and Landsat Data. Photogrammetric Engineering and Remote Sensing 53, 405–413.

Kiage, L.M., Walker, N.D., Balasubramanian, S., Babin, A., Barras, J., 2005. Applications of Radarsat-1 synthetic aperture radar imagery to assess hurricane-related flooding of coastal Louisiana. International Journal of Remote Sensing 26, 5359–5380. URL: https://www.tandfonline.com/doi/full/10.1080/01431160500442438, doi:10.1080/01431160500442438.

Kimutai, J., Vautard, R., Zachariah, M., Tolasz, R., Šustková, V., Cassou, C., Clarke, B., Haslinger, K., Vahlberg, M., Singh, R., Stephens, E., Cloke, H., Raju, E., Baumgart, N., Thalheimer, L., Otto, F., Koren, G., Philip, S., Kew, S., Haro, P., Vibert, J., Von Weissenberg, A., 2024. Climate change and high exposure increased costs and disruption to lives and livelihoods from flooding associated with exceptionally heavy rainfall in Central Europe. Technical Report. Imperial College London. URL: http://spiral.imperial.ac.uk/handle/10044/1/114694, doi:10.25561/114694.

Kittler, J., Illingworth, J., 1986. Minimum error thresholding. Pattern Recognition 19, 41–47. URL: https://linkinghub.elsevier.com/retrieve/pii/0031320386900300, doi:10.1016/0031-3203(86)90030-0.

Krullikowski, C., Chow, C., Wieland, M., Martinis, S., Bauer-Marschallinger, B., Roth, F., Matgen, P., Chini, M., Hostache, R., Li, Y., Salamon, P., 2023. Estimating Ensemble Likelihoods for the Sentinel-1-Based Global Flood Monitoring Product of the Copernicus Emergency Management Service. IEEE Journal of Selected Topics in Applied Earth Observations and Remote Sensing 16, 6917–6930. URL: https://ieeexplore.ieee.org/document/10186373/, doi:10.1109/JSTARS.2023.3292350.

Lahsaini, M., Albano, F., Albano, R., Mazzariello, A., Lacava, T., 2024. A Synthetic Aperture Radar-Based Robust Satellite Technique (RST) for Timely Mapping of Floods. Remote Sensing 16, 2193. URL: https://www.mdpi.com/2072-4292/16/12/2193, doi:10.3390/rs16122193.

Landuyt, L., Van Wesemael, A., Schumann, G.J.P., Hostache, R., Verhoest, N.E.C., Van Coillie, F.M.B., 2019. Flood Mapping Based on Synthetic Aperture Radar: An Assessment of Established Approaches. IEEE Transactions on Geoscience and Remote Sensing 57, 722–739. URL: https://ieeexplore.ieee.org/document/8432448/, doi:10.1109/TGRS.2018.2860054.

Landwehr, T., Dasgupta, A., Waske, B., 2024. Towards robust validation strategies for EO flood maps. Remote Sensing of Environment 315, 114439. URL: https://linkinghub.elsevier.com/retrieve/pii/S0034425724004656, doi:10.1016/j.rse.2024.114439.

Lewis, A.J., 1998. Geomorphic and Hydrologic Applications of Active Microwave Remote Sensing, in: Principles & Applications of Imaging Radar. third edition ed.. John Wiley & Sons, New York. volume 2 of *Manual of Remote Sensing*, pp. 567–629.

Li, S., Sun, D., Goldberg, M.D., Sjoberg, B., Santek, D., Hoffman, J.P., DeWeese, M., Restrepo, P., Lindsey, S., Holloway, E., 2018a. Automatic near real-time flood detection using Suomi-NPP/VIIRS data. Remote Sensing of Environment 204, 672–689. URL: https://linkinghub.elsevier.com/retrieve/pii/S0034425717304431, doi:10.1016/j.rse.2017.09.032.

Li, Y., Martinis, S., Plank, S., Ludwig, R., 2018b. An automatic change detection approach for rapid flood mapping in Sentinel-1 SAR data. International Journal of Applied Earth Observation and Geoinformation 73, 123–135. URL: https://www.sciencedirect.com/science/article/pii/S0303243418302782, doi:10.1016/j.jag.2018.05.023.

Long, S., Fatoyinbo, T.E., Policelli, F., 2014. Flood extent mapping for Namibia using change detection and thresholding with SAR. Environmental Research Letters 9, 035002. URL: https://iopscience.iop.org/article/10.1088/1748-9326/9/3/035002, doi:10.1088/1748-9326/9/3/035002.

Manavalan, R., 2017. SAR image analysis techniques for flood area mapping - literature survey. Earth Science Informatics 10, 1–14. URL: http://link.springer.com/10.1007/s12145-016-0274-2, doi:10.1007/s12145-016-0274-2.

Marconcini, M., Metz-Marconcini, A., Üreyen, S., Palacios-Lopez, D., Hanke, W., Bachofer, F., Zeidler, J., Esch, T., Gorelick, N., Kakarla, A., Paganini, M., Strano, E., 2020. Outlining where humans live, the World Settlement Footprint 2015. Scientific Data 7, 242. URL: https://www.nature.com/articles/s41597-020-00580-5, doi:10.1038/s41597-020-00580-5.

Martinis, S., Groth, S., Wieland, M., Knopp, L., Rättich, M., 2022. Towards a global seasonal and permanent reference water product from Sentinel-1/2 data for improved flood mapping. Remote Sensing of Environment 278, 113077. URL: https://linkinghub.elsevier.com/retrieve/pii/S0034425722001912, doi:10.1016/j.rse.2022.113077.

Martinis, S., Kersten, J., Twele, A., 2015. A fully automated TerraSAR-X based flood service. ISPRS Journal of Photogrammetry and Remote Sensing 104, 203–212. URL: https://linkinghub.elsevier.com/retrieve/pii/S0924271614001981, doi:10.1016/j.isprsjprs.2014.07.014.

Martinis, S., Plank, S., Ćwik, K., 2018. The Use of Sentinel-1 Time-Series Data to Improve Flood Monitoring in Arid Areas. Remote Sensing 10, 583. URL: https://www.mdpi.com/2072-4292/10/4/583, doi:10.3390/rs10040583.

Martinis, S., Twele, A., Voigt, S., 2009. Towards operational near real-time flood detection using a split-based automatic thresholding procedure on high resolution TerraSAR-X data. Natural Hazards and Earth System Sciences 9, 303–314. URL: https://nhess.copernicus.org/articles/9/303/2009/, doi:10.5194/nhess-9-303-2009.

Martinis, S., Wieland, M., Groth, S., 2024. A Multi-Sensor System for Surface Water Extraction: Application Examples in the Context of Disaster Management, in: IGARSS 2024 - 2024 IEEE International Geoscience and Remote Sensing Symposium, IEEE, Athens, Greece. pp. 1354–1357. URL: https://ieeexplore.ieee.org/document/10640717/, doi:10.1109/IGARSS53475.2024.10640717.

Mason, D., Giustarini, L., Garcia-Pintado, J., Cloke, H., 2014. Detection of flooded urban areas in high resolution Synthetic Aperture Radar images using double scattering. International Journal of Applied Earth Observation and Geoinformation 28, 150–159. URL: https://linkinghub.elsevier.com/retrieve/pii/S0303243413001700, doi:10.1016/j.jag.2013.12.002.

Mason, D.C., Dance, S.L., Vetra-Carvalho, S., Cloke, H.L., 2018. Robust algorithm for detecting floodwater in urban areas using synthetic aperture radar images. Journal of Applied Remote Sensing 12, 1. URL: https://www.spiedigitallibrary.org/journals/journal-of-applied-remote-sensing/volume-12/issue-04/045011/Robust-algorithm-for-detecting-floodwater-in-urban-areas-using-synthetic/10.1117/1.JRS.12.045011.full, doi:10.1117/1.JRS.12.045011.

Matgen, P., Hostache, R., Schumann, G., Pfister, L., Hoffmann, L., Savenije, H., 2011. Towards an automated SAR-based flood monitoring system: Lessons learned from two case studies. Physics and Chemistry of the Earth, Parts A/B/C 36, 241–252. URL: https://linkinghub.elsevier.com/retrieve/pii/S1474706510002160, doi:10.1016/j.pce.2010.12.009.

Matgen, P., Martinis, S., Wagner, W., Freeman, V., Zeil, P., McCormick, N., 2019. Feasibility assessment of an automated, global, satellite-based flood monitoring product for the Copernicus Emergency Management Service. Technical Report JRC116163. European Commission Joint Research Centre. Ispra, Italy. URL: https://data.europa.eu/doi/10.2760/653891.

Matthews, G., Baugh, C., Barnard, C., Carton De Wiart, C., Colonese, J., Grimaldi, S., Ham, D., Hansford, E., Harrigan, S., Heiselberg, S., Hooker, H., Hossain, S., Mazzetti, C., Milano, L., Moschini, F., O'Regan, K., Pappenberger, F., Pfister, D., Rajbhandari, R.M., Salamon, P., Ramos, A., Shelton, K., Stephens, E., Tasev, D., Turner, M., Van Den Homberg, M., Wittig, J., Zsótér, E., Prudhomme, C., 2025a. On the operational implementation of the Global Flood Awareness System (GloFAS), in: Flood Forecasting. Elsevier, pp. 299–350. URL: https://linkinghub.elsevier.com/retrieve/pii/B9780443140099000146, doi:10.1016/B978-0-443-14009-9.00014-6.

Matthews, G., Baugh, C., Barnard, C., De Wiart, C.C., Colonese, J., Decremer, D., Grimaldi, S., Hansford, E., Mazzetti, C., O'Regan, K., Pappenberger, F., Ramos, A., Salamon, P., Tasev, D., Prudhomme, C., 2025b. On the operational implementation of the European Flood Awareness System (EFAS), in: Flood Forecasting. Elsevier, pp. 251–298. URL: https://linkinghub.elsevier.com/retrieve/pii/B9780443140099000055, doi:10.1016/B978-0-443-14009-9.00005-5.

Meadows, P., Laur, H., Rosich, B., Schättler, B., 2001. The ERS-1 SAR Performance: A Final Update, in: CEOS SAR Workshop 2001 Proceedings, NASDA/EORC.

Metzger, M.J., Bunce, R.G.H., Jongman, R.H.G., Sayre, R., Trabucco, A., Zomer, R., 2013. A high-resolution bioclimate map of the world: a unifying framework for global biodiversity research and monitoring. Global Ecology and Biogeography 22, 630–638. URL: https://onlinelibrary.wiley.com/doi/10.1111/geb.12022, doi:10.1111/geb.12022.

Misra, A., White, K., Nsutezo, S.F., Straka, W., Lavista, J., 2024. Mapping Global Floods with 10 Years of Satellite Radar Data. URL: https://arxiv.org/abs/2411.01411, doi:10.48550/ARXIV.2411.01411. version Number: 1.

Morrow, R., Blurmstein, D., Dibarboure, G., 2018. Fine-scale Altimetry and the Future SWOT Mission, in: Chassignet, E.P., Pascual, A., Tintoré, J., Verron, J. (Eds.), New Frontiers in Operational Oceanography. GODAE Ocean-

View. URL: http://purl.flvc.org/fsu/fd/FSU_libsubv1_scholarship_submission_1536170512_b3d57dea, doi:10.17125/gov2018.ch08.

Mostafiz, R.B., Rohli, R.V., Friedland, C.J., Lee, Y.C., 2022. Actionable Information in Flood Risk Communications and the Potential for New Web-Based Tools for Long-Term Planning for Individuals and Community. Frontiers in Earth Science 10, 840250. URL: https://www.frontiersin.org/articles/10.3389/feart.2022.840250/full, doi:10.3389/feart.2022.840250.

Mullissa, A., Vollrath, A., Odongo-Braun, C., Slagter, B., Balling, J., Gou, Y., Gorelick, N., Reiche, J., 2021. Sentinel-1 SAR Backscatter Analysis Ready Data Preparation in Google Earth Engine. Remote Sensing 13, 1954. URL: https://www.mdpi.com/2072-4292/13/10/1954, doi:10.3390/rs13101954.

Nagler, T., Rott, H., 2000. Retrieval of wet snow by means of multitemporal SAR data. IEEE Transactions on Geoscience and Remote Sensing 38, 754–765. URL: http://ieeexplore.ieee.org/document/842004/, doi:10.1109/36.842004.

NASA JPL, 2013. NASA Shuttle Radar Topography Mission Water Body Data Shapefiles and Raster Files. URL: https://lpdaac.usgs.gov/products/srtmswbdv003/, doi:10.5067/MEASURES/SRTM/SRTMSWBD.003.

Navacchi, C., Cao, S., Bauer-Marschallinger, B., Snoeij, P., Small, D., Wagner, W., 2022. Utilising Sentinel-1's orbital stability for efficient pre-processing of sigma nought backscatter. ISPRS Journal of Photogrammetry and Remote Sensing 192, 130–141. URL: https://linkinghub.elsevier.com/retrieve/pii/S0924271622002003, doi:10.1016/j.isprsjprs.2022.07.023.

Nguyen, D.B., Wagner, W., 2017. European Rice Cropland Mapping with Sentinel-1 Data: The Mediterranean Region Case Study. Water 9, 392. URL: https://www.mdpi.com/2073-4441/9/6/392, doi:10.3390/w9060392. number: 6 Publisher: Multidisciplinary Digital Publishing Institute.

Oberstadler, R., Hönsch, H., Huth, D., 1997. Assessment of the mapping capabilities of ERS-1 SAR data for flood mapping: a case study in Germany. Hydrological Processes 11, 1415–1425. URL: https://onlinelibrary.wiley.com/doi/10.1002/(SICI)1099-1085(199708)11:10<1415::AID-HYP532>3.0.CO;2-2, doi:10.1002/(SICI)1099-1085(199708)11:10<1415::AID-HYP532>3.0.CO;2-2.

O'Grady, D., Leblanc, M., Gillieson, D., 2011. Use of ENVISAT ASAR Global Monitoring Mode to complement optical data in the mapping of rapid

broad-scale flooding in Pakistan. Hydrology and Earth System Sciences 15, 3475–3494. URL: https://hess.copernicus.org/articles/15/3475/2011/, doi:10.5194/hess-15-3475-2011.

Ohki, M., Takakura, Y., Kawakita, S., Tadono, T., 2024. ALOS-2 disaster mapping algorithms and their implementation in an operational system, in: 15th European Conference on Synthetic Aperture Radar (EUSAR 2024), VDE, Munich, Germany. pp. 779–781. URL: https://ieeexplore.ieee.org/abstract/document/10659532.

Olofsson, P., Foody, G.M., Herold, M., Stehman, S.V., Woodcock, C.E., Wulder, M.A., 2014. Good practices for estimating area and assessing accuracy of land change. Remote Sensing of Environment 148, 42–57. URL: https://linkinghub.elsevier.com/retrieve/pii/S0034425714000704, doi:10.1016/j.rse.2014.02.015.

Paprotny, D., Sebastian, A., Morales-Nápoles, O., Jonkman, S.N., 2018. Trends in flood losses in Europe over the past 150 years. Nature Communications 9, 1985. URL: https://www.nature.com/articles/s41467-018-04253-1, doi:10.1038/s41467-018-04253-1.

Park, S.E., Bartsch, A., Sabel, D., Wagner, W., Naeimi, V., Yamaguchi, Y., 2011. Monitoring freeze/thaw cycles using ENVISAT ASAR Global Mode. Remote Sensing of Environment 115, 3457–3467. URL: https://linkinghub.elsevier.com/retrieve/pii/S0034425711002914, doi:10.1016/j.rse.2011.08.009.

Pekel, J.F., Cottam, A., Gorelick, N., Belward, A.S., 2016. High-resolution mapping of global surface water and its long-term changes. Nature 540, 418–422. URL: https://www.nature.com/articles/nature20584, doi:10.1038/nature20584.

Potin, P., Bargellini, P., Laur, H., Rosich, B., Schmuck, S., 2012. Sentinel-1 mission operations concept, in: 2012 IEEE International Geoscience and Remote Sensing Symposium, IEEE, Munich, Germany. pp. 1745–1748. URL: http://ieeexplore.ieee.org/document/6351183/, doi:10.1109/IGARSS.2012.6351183.

Pulvirenti, L., Marzano, F.S., Pierdicca, N., Mori, S., Chini, M., 2014. Discrimination of Water Surfaces, Heavy Rainfall, and Wet Snow Using COSMO-SkyMed Observations of Severe Weather Events. IEEE Transactions on Geoscience and Remote Sensing 52, 858–869. URL: http://ieeexplore.ieee.org/document/6488761/, doi:10.1109/TGRS.2013.2244606.

Quast, R., Wagner, W., Bauer-Marschallinger, B., Vreugdenhil, M., 2023. Soil moisture retrieval from Sentinel-1 using a first-order radiative transfer model—A case-study over the Po-Valley. Remote Sensing of Environment 295, 113651. URL: https://linkinghub.elsevier.com/retrieve/pii/S003442572300202X, doi:10.1016/j.rse.2023.113651.

Rahman, M.R., Thakur, P.K., 2018. Detecting, mapping and analysing of flood water propagation using synthetic aperture radar (SAR) satellite data and GIS: A case study from the Kendrapara District of Orissa State of India. The Egyptian Journal of Remote Sensing and Space Science 21, S37–S41. URL: https://linkinghub.elsevier.com/retrieve/pii/S1110982317301126, doi:10.1016/j.ejrs.2017.10.002.

Raney, R.K., Luscombe, A.P., Langham, E.J., Ahmed, S., 1991. Radarsat. Proceedings of the IEEE 79, 839–849.

Rees, W.G., 2000. Technical note: Simple masks for shadowing and highlighting in SAR images. International Journal of Remote Sensing 21, 2145–2152. URL: https://www.tandfonline.com/doi/full/10.1080/01431160050029477, doi:10.1080/01431160050029477.

Refice, A., Zingaro, M., D'Addabbo, A., Chini, M., 2020. Integrating C- and L-Band SAR Imagery for Detailed Flood Monitoring of Remote Vegetated Areas. Water 12, 2745. URL: https://www.mdpi.com/2073-4441/12/10/2745, doi:10.3390/w12102745.

Rennó, C.D., Nobre, A.D., Cuartas, L.A., Soares, J.V., Hodnett, M.G., Tomasella, J., Waterloo, M.J., 2008. HAND, a new terrain descriptor using SRTM-DEM: Mapping terra-firme rainforest environments in Amazonia. Remote Sensing of Environment 112, 3469–3481. URL: https://linkinghub.elsevier.com/retrieve/pii/S003442570800120X, doi:10.1016/j.rse.2008.03.018.

Reuß, F., Navacchi, C., Greimeister-Pfeil, I., Vreugdenhil, M., Schaumberger, A., Klingler, A., Mayer, K., Wagner, W., 2024. Evaluation of limiting factors for SAR backscatter based cut detection of alpine grasslands. Science of Remote Sensing , 100117URL: https://linkinghub.elsevier.com/retrieve/pii/S2666017224000014, doi:10.1016/j.srs.2024.100117.

Rosen, P.A., Kumar, R., 2021. NASA-ISRO SAR (NISAR) Mission Status, in: 2021 IEEE Radar Conference (RadarConf21), IEEE, Atlanta, GA, USA. pp. 1–6. URL: https://ieeexplore.ieee.org/document/9455211/, doi:10.1109/RadarConf2147009.2021.9455211.

Rossi, C., Acerbo, F., Ylinen, K., Juga, I., Nurmi, P., Bosca, A., Tarasconi, F., Cristoforetti, M., Alikadic, A., 2018. Early detection and information extraction for weather-induced floods using social media streams. International Journal of Disaster Risk Reduction 30, 145–157. URL: https://linkinghub.elsevier.com/retrieve/pii/S2212420918302735, doi:10.1016/j.ijdrr.2018.03.002.

Roth, F., Bauer-Marschallinger, B., Tupas, M.E., Reimer, C., Salamon, P., Wagner, W., 2023. Sentinel-1-based analysis of the severe flood over Pakistan 2022. Natural Hazards and Earth System Sciences 23, 3305–3317. URL: https://nhess.copernicus.org/articles/23/3305/2023/, doi:10.5194/nhess-23-3305-2023.

Roth, F., Tupas, M., Navacchi, C., Zhao, J., Wagner, W., Bauer-Marschallinger, B., 2025. Evaluating the robustness of Bayesian flood mapping with Sentinel-1 data: a multi- event validation study. Science of Remote Sensing in review.

Salamon, P., Mctlormick, N., Reimer, C., Clarke, T., Bauer-Marschallinger, B., Wagner, W., Martinis, S., Chow, C., Bohnke, C., Matgen, P., Chini, M., Hostache, R., Molini, L., Fiori, E., Walli, A., 2021. The New, Systematic Global Flood Monitoring Product of the Copernicus Emergency Management Service, in: 2021 IEEE International Geoscience and Remote Sensing Symposium IGARSS, IEEE, Brussels, Belgium. pp. 1053–1056. URL: https://ieeexplore.ieee.org/document/9554214/, doi:10.1109/IGARSS47720.2021.9554214.

Santoro, M., Cartus, O., 2018. Research Pathways of Forest Above-Ground Biomass Estimation Based on SAR Backscatter and Interferometric SAR Observations. Remote Sensing 10, 608. URL: https://www.mdpi.com/2072-4292/10/4/608, doi:10.3390/rs10040608.

Schiavina, M., Freire, S., MacManus, K., 2023. GHS-POP R2023A - GHS population grid multitemporal (1975-2030). URL: http://data.europa.eu/89h/2ff68a52-5b5b-4a22-8f40-c41da8332cfe, doi:10.2905/2FF68A52-5B5B-4A22-8F40-C41DA8332CFE.

Schlaffer, S., Chini, M., Dettmering, D., Wagner, W., 2016. Mapping Wetlands in Zambia Using Seasonal Backscatter Signatures Derived from ENVISAT ASAR Time Series. Remote Sensing 8, 402. URL: http://www.mdpi.com/2072-4292/8/5/402, doi:10.3390/rs8050402.

Schlaffer, S., Chini, M., Giustarini, L., Matgen, P., 2017. Probabilistic mapping of flood-induced backscatter changes in SAR time se-

ries. International Journal of Applied Earth Observation and Geoinformation 56, 77–87. URL: https://linkinghub.elsevier.com/retrieve/pii/S0303243416301994, doi:10.1016/j.jag.2016.12.003.

Schlaffer, S., Matgen, P., Hollaus, M., Wagner, W., 2015. Flood detection from multi-temporal SAR data using harmonic analysis and change detection. International Journal of Applied Earth Observation and Geoinformation 38, 15–24. URL: https://linkinghub.elsevier.com/retrieve/pii/S0303243414002645, doi:10.1016/j.jag.2014.12.001.

Seewald, M., Gruber, C., Innerbichler, F., Pasik, A., Duffy, C., Riffler, M., Reimer, C., Stachl, T., Kidd, R., McCormick, N., Salamon, P., Europäische Kommission, Copernicus (Eds.), 2024. Global flood monitoring: annual product and service quality assessment report 2023. Number 32022 in EUR, Publications Office of the European Union, Luxembourg. doi:10.2760/41122.

Small, D., 2011. Flattening Gamma: Radiometric Terrain Correction for SAR Imagery. IEEE Transactions on Geoscience and Remote Sensing 49, 3081–3093. doi:10.1109/TGRS.2011.2120616.

Solbo, S., Solheim, I., 2004. Towards operational flood mapping with satellite SAR, in: Proeedings of the 2004 ENVISAT & ERS Symposium, European Space Agency, Salzburg, Austria. pp. 1–7.

Stehman, S.V., Czaplewski, R.L., 1998. Design and Analysis for Thematic Map Accuracy Assessment. Remote Sensing of Environment 64, 331–344. URL: https://linkinghub.elsevier.com/retrieve/pii/S0034425798000108, doi:10.1016/S0034-4257(98)00010-8.

Torres, R., Geudtner, D., Davidson, M., Bibby, D., Navas-Traver, I., Garcia Hernandez, A.I., Laduree, G., Poupaert, J., Bollian, T., Graham, S., 2024. Sentinel-1 Next Generation: Enhanced C-band Data Continuity, in: 15th European Conference on Synthetic Aperture Radar (EUSAR 2024), VDE, Munich, Germany. pp. 1–4. URL: https://ieeexplore.ieee.org/abstract/document/10659647/.

Torres, R., Snoeij, P., Geudtner, D., Bibby, D., Davidson, M., Attema, E., Potin, P., Rommen, B., Floury, N., Brown, M., Traver, I.N., Deghaye, P., Duesmann, B., Rosich, B., Miranda, N., Bruno, C., L'Abbate, M., Croci, R., Pietropaolo, A., Huchler, M., Rostan, F., 2012. GMES Sentinel-1 mission. Remote Sensing of Environment 120, 9–24. URL: https://linkinghub.elsevier.com/retrieve/pii/S0034425712000600, doi:10.1016/j.rse.2011.05.028.

Tradowsky, J.S., Philip, S.Y., Kreienkamp, F., Kew, S.F., Lorenz, P., Arrighi, J., Bettmann, T., Caluwaerts, S., Chan, S.C., De Cruz, L., De Vries, H., Demuth, N., Ferrone, A., Fischer, E.M., Fowler, H.J., Goergen, K., Heinrich, D., Henrichs, Y., Kaspar, F., Lenderink, G., Nilson, E., Otto, F.E.L., Ragone, F., Seneviratne, S.I., Singh, R.K., Skålevåg, A., Termonia, P., Thalheimer, L., Van Aalst, M., Van Den Bergh, J., Van De Vyver, H., Vannitsem, S., Van Oldenborgh, G.J., Van Schaeybroeck, B., Vautard, R., Vonk, D., Wanders, N., 2023. Attribution of the heavy rainfall events leading to severe flooding in Western Europe during July 2021. Climatic Change 176, 90. URL: https://link.springer.com/10.1007/s10584-023-03502-7, doi:10.1007/s10584-023-03502-7.

Tsyganskaya, V., Martinis, S., Marzahn, P., Ludwig, R., 2018. SAR-based detection of flooded vegetation – a review of characteristics and approaches. International Journal of Remote Sensing 39, 2255–2293. URL: https://www.tandfonline.com/doi/full/10.1080/01431161.2017.1420938, doi:10.1080/01431161.2017.1420938.

Tupas, M.E., Roth, F., Bauer-Marschallinger, B., Wagner, W., 2023a. Improving Sentinel-1 Flood Maps Using a Topographic Index as Prior in Bayesian Inference. Water 15, 4034. URL: https://www.mdpi.com/2073-4441/15/23/4034, doi:10.3390/w15234034.

Tupas, M.E., Roth, F., Bauer-Marschallinger, B., Wagner, W., 2023b. An Intercomparison of Sentinel-1 Based Change Detection Algorithms for Flood Mapping. Remote Sensing 15, 1200. URL: https://www.mdpi.com/2072-4292/15/5/1200, doi:10.3390/rs15051200.

Tupas, M.E., Roth, F., Bauer-Marschallinger, B., Wagner, W., 2024. Assessment of time-series-derived no-flood references for SAR-based Bayesian flood mapping. GIScience & Remote Sensing 61, 2427304. URL: https://www.tandfonline.com/doi/full/10.1080/15481603.2024.2427304, doi:10.1080/15481603.2024.2427304.

Twele, A., Cao, W., Plank, S., Martinis, S., 2016. Sentinel-1-based flood mapping: a fully automated processing chain. International Journal of Remote Sensing 37, 2990–3004. URL: https://www.tandfonline.com/doi/full/10.1080/01431161.2016.1192304, doi:10.1080/01431161.2016.1192304.

Velastegui-Montoya, A., Montalván-Burbano, N., Carrión-Mero, P., Rivera-Torres, H., Sadeck, L., Adami, M., 2023. Google Earth Engine: A Global Analysis

and Future Trends. Remote Sensing 15, 3675. URL: https://www.mdpi.com/2072-4292/15/14/3675, doi:10.3390/rs15143675.

Voigt, S., Kemper, T., Riedlinger, T., Kiefl, R., Scholte, K., Mehl, H., 2007. Satellite Image Analysis for Disaster and Crisis-Management Support. IEEE Transactions on Geoscience and Remote Sensing 45, 1520–1528. URL: http://ieeexplore.ieee.org/document/4215094/, doi:10.1109/TGRS.2007.895830.

Wagner, W., Bauer-Marschalling, B., Roth, F., Briese, C., Reimer, C., Lacaze, R., Moroz, M., Salamon, P., Davidson, M., 2024. Requirements from the Copernicus soil moisture and flood monitoring services for Sentinel-1 and ROSE-L mission operations, in: Proceedings of the 15th European Conference on Synthetic Aperture Radar (EUSAR 2024), VDE Verlag, Munich, Germany. pp. 114–118. URL: https://ieeexplore.ieee.org/abstract/document/10659679.

Wagner, W., Bauer-Marschallinger, B., Navacchi, C., Reuß, F., Cao, S., Reimer, C., Schramm, M., Briese, C., 2021. A Sentinel-1 Backscatter Datacube for Global Land Monitoring Applications. Remote Sensing 13, 4622. URL: https://www.mdpi.com/2072-4292/13/22/4622, doi:10.3390/rs13224622.

Wagner, W., Freeman, V., Cao, S., Matgen, P., Chini, M., Salamon, P., McCormick, N., Martinis, S., Bauer-Marschallinger, B., Navacchi, C., Schramm, M., Reimer, C., Briese, C., 2020. Data processing architectures for monitoring floods using Sentinel-1, in: ISPRS Annals of the Photogrammetry, Remote Sensing and Spatial Information Sciences, Copernicus GmbH. pp. 641–648. URL: https://www.isprs-ann-photogramm-remote-sens-spatial-inf-sci.net/V-3-2020/641/2020/, doi:10.5194/isprs-annals-V-3-2020-641-2020. iSSN: 2194-9042.

Wagner, W., Lindorfer, R., Melzer, T., Hahn, S., Bauer-Marschallinger, B., Morrison, K., Calvet, J.C., Hobbs, S., Quast, R., Greimeister-Pfeil, I., Vreugdenhil, M., 2022. Widespread occurrence of anomalous C-band backscatter signals in arid environments caused by subsurface scattering. Remote Sensing of Environment 276, 113025. URL: https://linkinghub.elsevier.com/retrieve/pii/S0034425722001390, doi:10.1016/j.rse.2022.113025.

Wang, Y., 2004. Seasonal change in the extent of inundation on floodplains detected by JERS-1 Synthetic Aperture Radar data. International Journal of Remote Sensing 25, 2497–2508. URL: https://www.tandfonline.com/doi/full/10.1080/01431160310001619562, doi:10.1080/01431160310001619562.

Wang, Z., Zhang, C., Atkinson, P.M., 2022. Combining SAR images with land cover products for rapid urban flood mapping. Frontiers in Environmental Science 10, 973192. URL: https://www.frontiersin.org/articles/10.3389/fenvs.2022.973192/full, doi:10.3389/fenvs.2022.973192.

Wania, A., Joubert-Boitat, I., Dottori, F., Kalas, M., Salamon, P., 2021. Increasing Timeliness of Satellite-Based Flood Mapping Using Early Warning Systems in the Copernicus Emergency Management Service. Remote Sensing 13, 2114. URL: https://www.mdpi.com/2072-4292/13/11/2114, doi:10.3390/rs13112114.

Wieland, M., Martinis, S., 2019. A Modular Processing Chain for Automated Flood Monitoring from Multi-Spectral Satellite Data. Remote Sensing 11, 2330. URL: https://www.mdpi.com/2072-4292/11/19/2330, doi:10.3390/rs11192330.

Wilks, D., 2011. Forecast Verification, in: International Geophysics. Elsevier. volume 100, pp. 301–394. URL: https://linkinghub.elsevier.com/retrieve/pii/B9780123850225000087, doi:10.1016/B978-0-12-385022-5.00008-7.

Zhang, M., Chen, F., Liang, D., Tian, B., Yang, A., 2020. Use of Sentinel-1 GRD SAR Images to Delineate Flood Extent in Pakistan. Sustainability 12, 5784. URL: https://www.mdpi.com/2071-1050/12/14/5784, doi:10.3390/su12145784.

Zhao, J., Li, M., Li, Y., Matgen, P., Chini, M., 2025. Urban Flood Mapping Using Satellite Synthetic Aperture Radar Data: A review of characteristics, approaches, and datasets. IEEE Geoscience and Remote Sensing Magazine , 2–34URL: https://ieeexplore.ieee.org/document/10795465/, doi:10.1109/MGRS.2024.3496075.

Zhao, J., Li, Y., Matgen, P., Pelich, R., Hostache, R., Wagner, W., Chini, M., 2022. Urban-Aware U-Net for Large-Scale Urban Flood Mapping Using Multitemporal Sentinel-1 Intensity and Interferometric Coherence. IEEE Transactions on Geoscience and Remote Sensing 60, 1–21. URL: https://ieeexplore.ieee.org/document/9857936/, doi:10.1109/TGRS.2022.3199036.

Zhao, J., Pelich, R., Hostache, R., Matgen, P., Cao, S., Wagner, W., Chini, M., 2021a. Deriving exclusion maps from C-band SAR time-series in support of floodwater mapping. Remote Sensing of Environment 265, 112668. URL: https://www.sciencedirect.com/science/article/pii/S0034425721003886, doi:10.1016/j.rse.2021.112668.

Zhao, J., Pelich, R., Hostache, R., Matgen, P., Wagner, W., Chini, M., 2021b. A large-scale 2005–2012 flood map record derived from ENVISAT-ASAR data: United Kingdom as a test case. Remote Sensing of Environment 256, 112338. URL: https://linkinghub.elsevier.com/retrieve/pii/S0034425721000560, doi:10.1016/j.rse.2021.112338.

Zhu, L., Walker, J.P., Ye, N., Rüdiger, C., 2019. Roughness and vegetation change detection: A pre-processing for soil moisture retrieval from multi-temporal SAR imagery. Remote Sensing of Environment 225, 93–106. URL: https://linkinghub.elsevier.com/retrieve/pii/S0034425719300823, doi:10.1016/j.rse.2019.02.027.

Tables and Figures

Algorithm	Single-image	Dual-image	Time-series
Developer	DLR	LIST	TU Wien
Target variables	Total water area	Total water and recently flooded area	Flood area compared to seasonal mean
Reference image	None	Last image from same orbit	Image simulated with harmonic model
Method	Hierarchical tile-based thresholding	Hierarchical split-based thresholding	Bayesian inference
Thresholds	Automatic tile-based thresholds for backscatter	Automatic tile-based thresholds for backscatter and backscatter change	Fixed threshold of Bayesian posteriori probability
Likelihood	Fuzzy logic	Bayesian inference	Bayesian inference
Post-processing	Region-growing	Region-growing	Noise filter
Main reference	Martinis et al. (2015)	Chini et al. (2017)	Bauer-Marschallinger et al. (2022)

Table 1: Main characteristics of the three flood mapping algorithms used within the GFM service.

Access	Description	Link
Web viewers	GFM viewers integrated into the web viewers of the Global Flood Awareness System (GloFAS) and the European Flood Awareness System (EFAS)	https://global-flood.emergency.copernicus.eu/ https://european-flood.emergency.copernicus.eu/
REST API	RESTful APIs written in Python with the Flask framework for web applications	https://api.gfm.eodc.eu/v2/
Web Map Service	GeoServer implementation to support web-based GIS analysis	https://geoserver.gfm.eodc.eu/geoserver/gfm/wms
Web portal	Dedicated webportal tailored for operational GFM applications	https://portal.gfm.eodc.eu/

Table 2: Access mechanisms for the GFM flood products.

Name	Description	Sections	Data Formats
Observed Flood extent	Flooded areas observed by Sentinel-1, mapped by applying a majority voting on three scientific algorithms	2.2, 2.2.4	Raster (COG) and vector (GeoJSON)
Total water extent	Total water extent by blending observed flood extent and reference water extent	2.2.4	Raster (COG) and vector (GeoJSON)
Reference water extent	Monthly maps of permanent and seasonal water extent derived from median Sentinel-1 backscatter images using the single- and dual-image algorithms	2.2, 2.3.1	Raster (COG) and vector (GeoJSON)
Exclusion mask	Unclassified areas due to topography and lack of sensitivity of Sentinel-1 (forests, cities, smooth surfaces)	2.3.2	Raster (COG)
Flood likelihood	Likelihood of a pixel being flooded derived by averaging the likelihoods from the three scientific algorithms	2.2.4	Raster (COG)
Advisory flags	Flags indicating potential misclassifications due to environmental conditions (dry soils, frost, snow, wind)	2.3.3	Raster (COG)
S-1 footprint & Metadata	Sentinel-1 acquisition parameters inherited from IW image	2.4.2	KML
S-1 schedule	Next scheduled Sentinel-1 acquisition	2.4.2	KML
Affected population	Number of people in affected areas, mapped by overlaying the flood map with population data	2.4.2	Raster (COG)
Affected land cover	Flood land cover classes, mapped by overlaying flood map with land cover data	2.4.2	Raster (COG)

Table 3: The ten data layers of the CEMS GFM product. COG stands for cloud optimised GeoTIFF, GeoJSON is a format for encoding a different geographic data structures, and KML is a file format used to display geographic data in Earth browsers.

Continent	Events	Detected	Missed	No Data
Europe	20	19	1	0
Asia	20	14	3	3
South America	20	14	4	2
Africa	20	13	7	0
North America	15	9	3	3
Oceania	9	4	3	2
Total	**104**	**73**	**21**	**10**

Table 4: Summary of flood events detection performance by continent.

Class	OA [%]	CSI [%]
Permanent water	95.9±0.2	64.1±0.7
Seasonal water	74.4±0.4	55.2±0.8
Flood	72.0±0.4	43.7±0.8

Table 5: Global evaluation results for permanent water, seasonal water, and flood pixels, showing Overall Accuracy (OA) and Critical Success Index (CSI) together with their 95% confidence intervals.

Biome	Environmental zone	No.	OA [%]	CSI [%]
Boreal/Alpine	E. Cold and wet	543	78.1±3.6	41.9±4.9
	F. Extremely cold and mesic	4521	69.7±1.4	57.5±1.7
	G. Cold and mesic	4542	80.9±1.2	64.2±1.6
Cool temperate	H. Cool temperate and dry	3931	77.2±1.4	58.3±1.8
	I. Cool temperate and xeric	3130	78.7±1.5	55.2±2.0
	J. Cool temperate and moist	1185	94.7±1.3	68.4±3.1
Warm temperate	K. Warm temperate and mesic	3273	92.9±0.9	63.8±1.9
	L. Warm temperate and xeric	3439	82.3±1.3	47.8±2.0
Sub-tropical	M. Hot and mesic	2286	89.4±1.3	63.7±2.3
Drylands	N. Hot and dry	4149	73.1±1.4	53.1±1.8
	O. Hot and arid	2319	64.2±2.1	36.2±2.3
	P. Extremely hot and arid	1412	67.2±2.6	37.4±3.0
	Q. Extremely hot and xeric	4875	79.2±1.2	59.4±1.6
Tropical	R. Extremely hot and moist	8458	85.8±0.8	74.2±1.1

Table 6: Evaluation results for different bio-geographic regions as defined by Metzger et al. (2013). The third column shows the number of sample points per environmental zone. Note that results from the arctic biome are not included in this table due to the small number of sample points (<100).

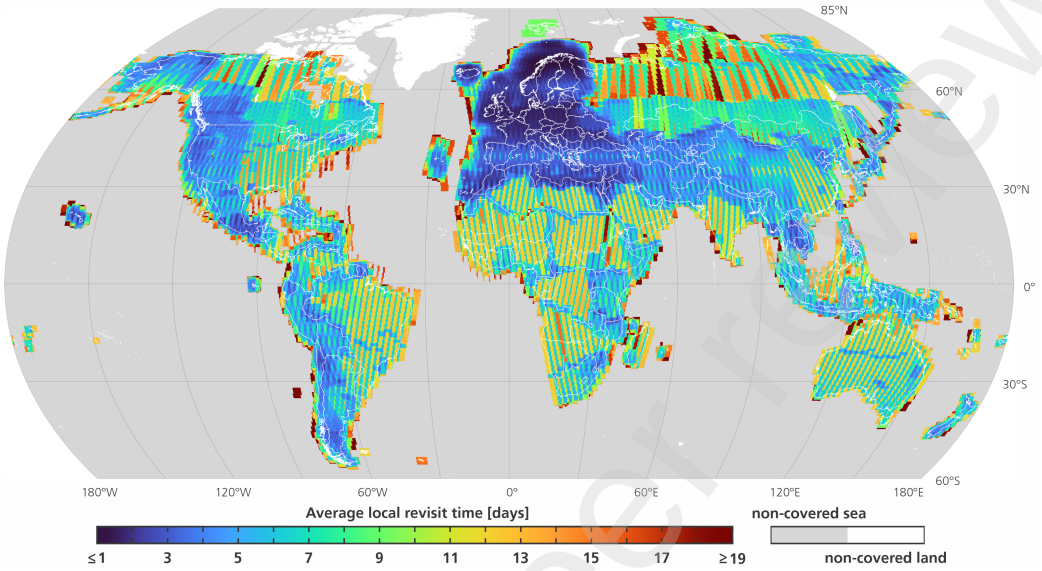

Figure 1: Average revisit time of the Sentinel-1 two-satellite constellation over non-polar land. The image was created by collecting all Interferometric Wide (IW) swath data acquired by Sentinel-1A and Sentinel-1B in the years from 2016 to 2021.

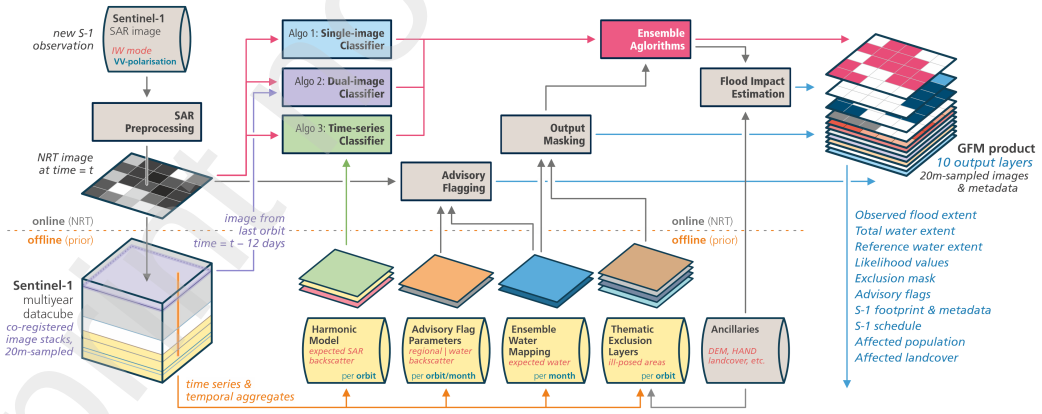

Figure 2: Overview of GFM's main algorithms and workflows, with NRT processes in the top, and offline model layer generation in the bottom.

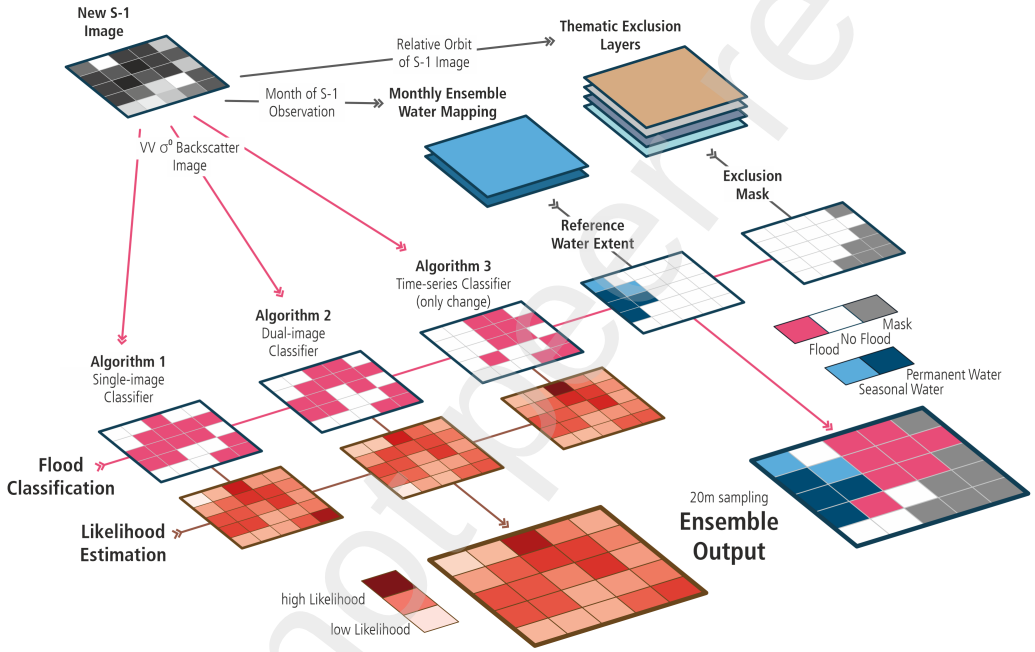

Figure 3: Illustration of the GFM ensemble approach for merging the flood maps and likelihood estimates produced by three independent flood mapping algorithms. Prior-computed monthly reference water maps and an exclusion mask are used for masking the ensemble flood map.

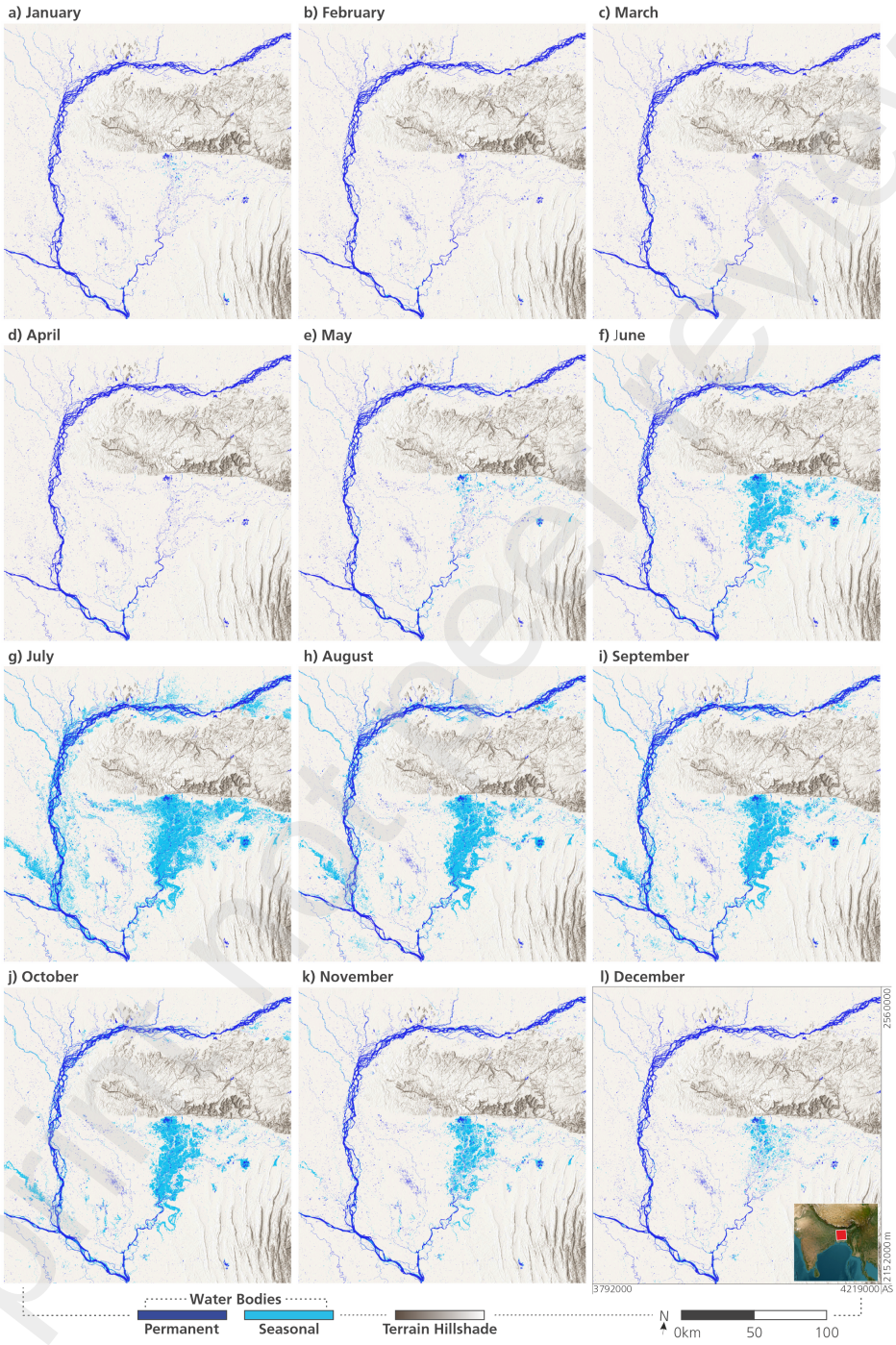

Figure 4: GFM's monthly reference water maps for Bangladesh, with permanent (dark blue) and seasonal water bodies (light blue).

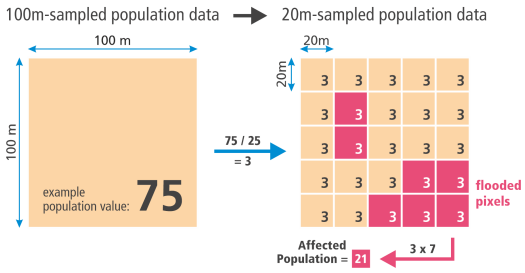

Figure 5: Illustration of the approach to estimate the number of affected people by superimposing the 100 m Global Human Settlement Layer with the 20 m GFM flood map.

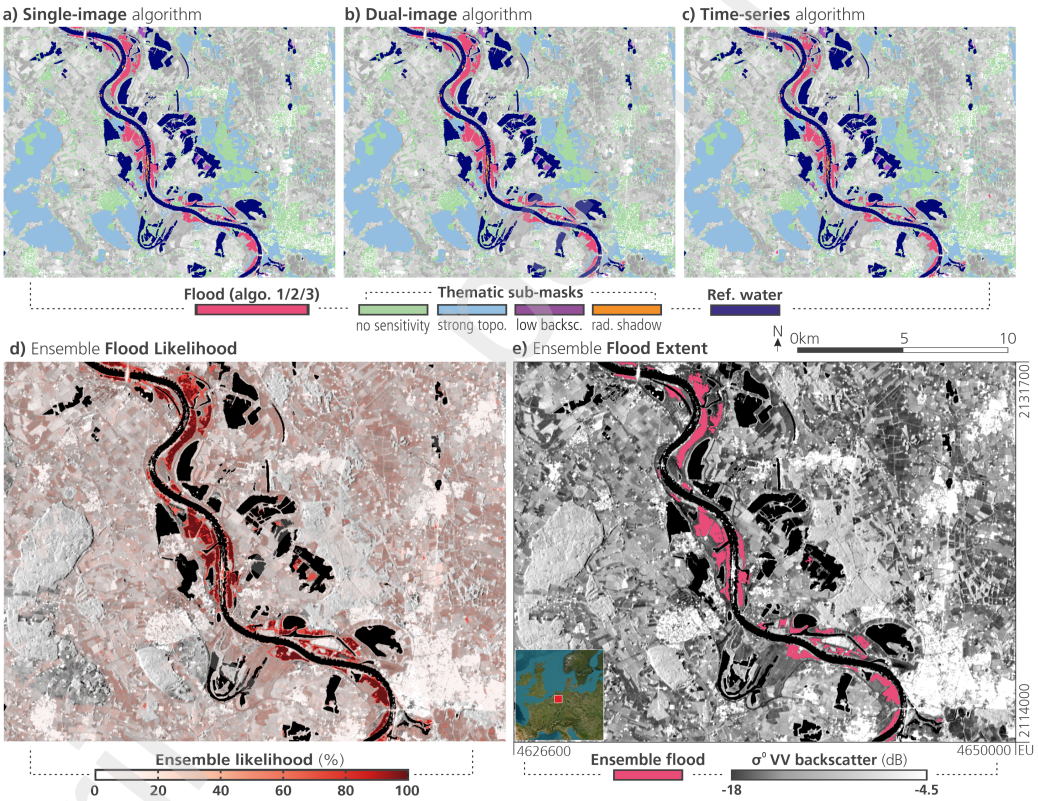

Figure 6: a)-c) show the thematic exclusion layers, the monthly reference water extent, and the individual floods maps from the three contributing scientific algorithms. The GFM ensemble output is shown with the flood likelihood in d), and the ensemble flood in e). The scene shows the flood situation on July 17, 2021, along the river Rhine in Germany, near the city of Wesel. The background shows the temporally aggregated VV backscatter from Sentinel-1 Global Backscatter Model from Bauer-Marschallinger et al. (2021).

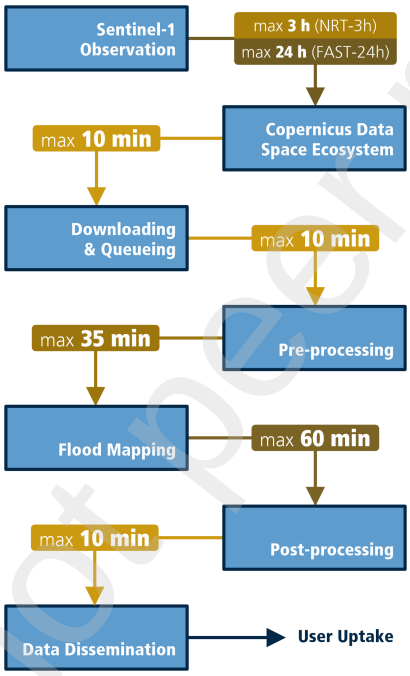

Figure 7: Timeliness of the GFM service, with maximum durations under regular conditions between acquisition from Copernicus, GFM main processing modules, and product dissemination. NRT-3h and FAST-24h refer to Copernicus' Sentinel-1 timeliness categories.

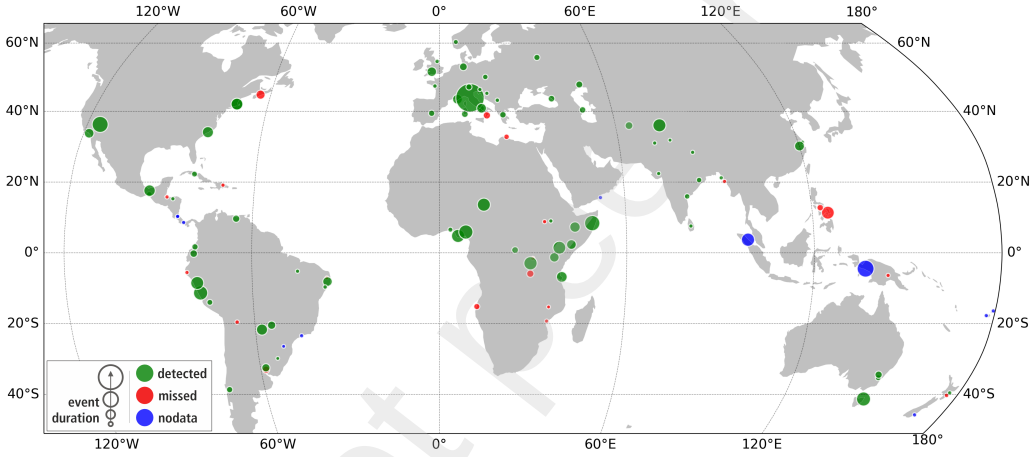

Figure 8: Overview on the coverage analysis of 104 flood events from 2022-2024 listed in Tab. 7. See results also in Tab. 4. Flood events are detected (green circles) or missed (red circles) by GFM with Sentinel-1A. The blue circles show cases where no Sentinel-1 image was acquired over the entire flood duration as reported in the GDACS database. The size of the circles illustrates event duration.

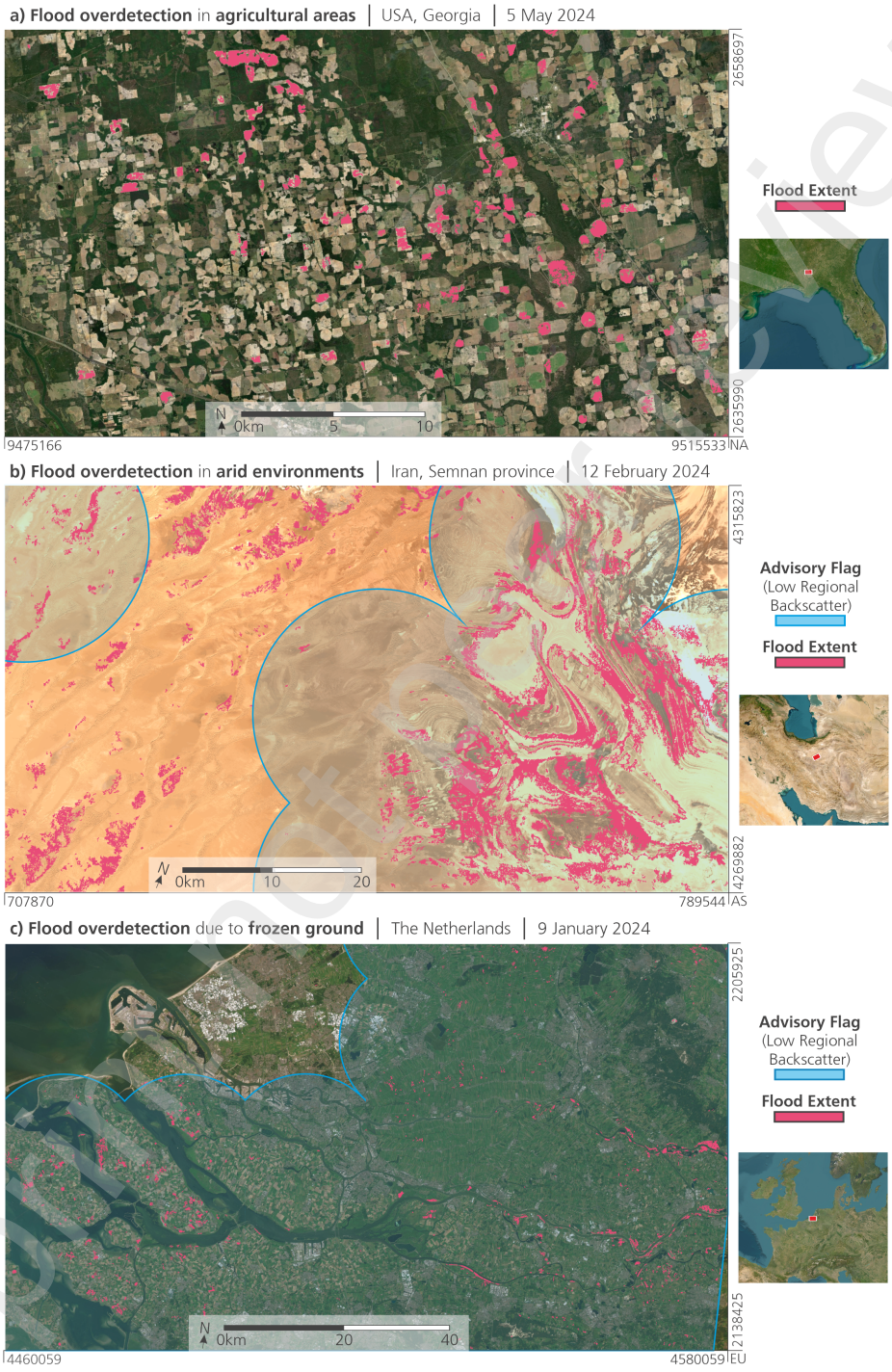

Figure 9: Examples of overdetection in non-flood situations: a) Agricultural areas in the USA, and b) dry soil in Iran. c) Shows in the Netherlands an actual flood event, but an exceptional one under frozen soils conditions. The GFM low regional backscatter advisory flag is displayed in transparent blue, indicating backscatter decrease at the larger scale.

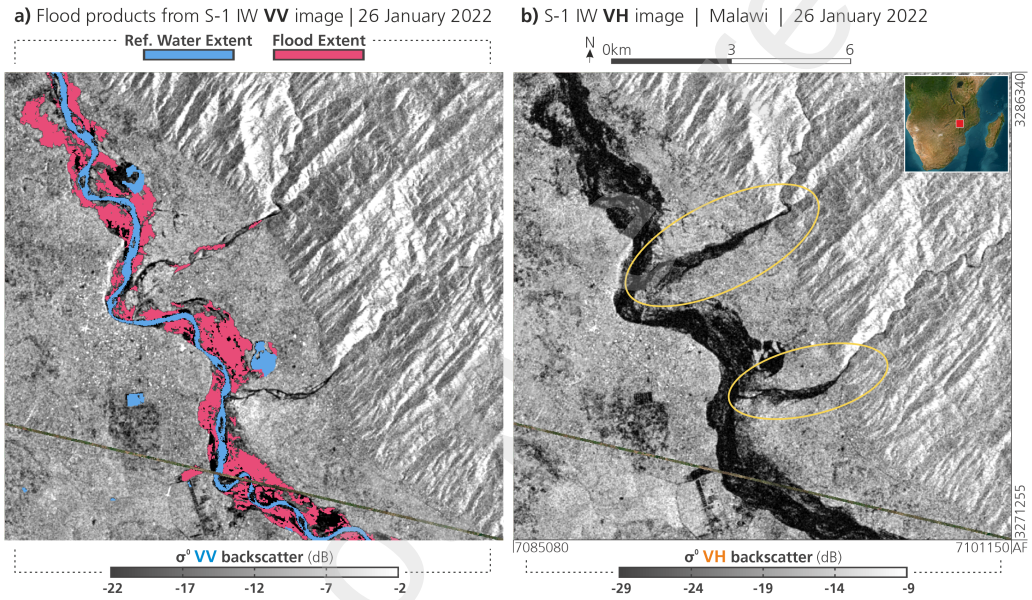

Figure 10: 2022 flood event in Malawi, an example for underdetection of flooded vegetation due to the limitation to a single polarisation (modified from Roth et al., submitted). a) shows the GFM products based on Sentinel-1 IW data in VV-polarisation; b) shows the VH band of the same dataset, with flooded areas underdetected in VV highlighted by yellow ellipses.

Table 7: Selected flood events from the GDACS flood events record (2022-2024).

ID	Country	From Date	To Date	GDACS Score	Deaths	Displaced
AF01	Libya	08-09-2023	14-09-2023	2.5	3500	33000
AF02	Nigeria	10-09-2022	26-10-2022	2.5	605	1306000
AF03	Chad	01-09-2024	17-10-2024	1.5	576	-
AF04	South Sudan	03-08-2024	05-08-2024	1.5	0	571989
AF05	Kenya	12-04-2024	06-05-2024	1.5	219	206000
AF06	Burundi	17-03-2024	03-05-2024	1.5	5	209486
AF07	Ethiopia	29-04-2024	01-05-2024	1.5	18	106193
AF08	Tanzania	28-03-2024	28-04-2024	1.5	169	1660
AF09	Ethiopia	07-11-2023	06-12-2023	1.5	53	347600
AF10	Kenya	23-10-2023	06-12-2023	1.5	136	462160
AF11	Somalia	04-10-2023	06-12-2023	1.5	87	458126
AF12	Democratic Republic of Congo	01-05-2023	10-05-2023	1.5	478	3300
AF13	Rwanda	01-05-2023	03-05-2023	1.5	109	-
AF14	Democratic Republic of Congo	01-04-2023	15-04-2023	1.5	20	100500
AF15	Somalia	20-03-2023	14-04-2023	1.5	30	140000
AF16	Malawi	13-03-2023	16-03-2023	1.5	225	88312
AF17	Mozambique	22-03-2024	24-03-2024	0.5	4	7658
AF18	Nigeria	14-10-2024	19-10-2024	0.5	25	5328
AF19	Nigeria	23-06-2024	23-09-2024	0.5	5	10284
AF20	Angola	25-11-2022	05-12-2022	0.5	15	405
AS01	India	20-10-2024	26-10-2024	2.5	9	803,888
AS02	Bangladesh, India, Myanmar	13-05-2023	15-05-2023	2.5	41	850,000
AS03	China, Taiwan	14-09-2022	16-09-2022	2.5	0	1,233,000
AS04	Pakistan	14-06-2022	31-08-2022	2.5	1,061	215,997
AS05	Nepal	26-09-2024	28-09-2024	1.5	148	-
AS06	India	30-08-2024	05-09-2024	0.5	45	45,369
AS07	Indonesia	03-02-2024	12-06-2024	1.5	79	84,943
AS08	Afghanistan	09-05-2024	25-05-2024	1.5	387	-
AS09	Kazakhstan	28-03-2024	10-04-2024	1.5	2	104,694
AS10	Bangladesh	24-10-2023	26-10-2023	1.5	3	273,000
AS11	Pakistan	16-08-2023	18-08-2023	1.5	0	100,000
AS12	China	27-06-2023	23-07-2023	1.5	15	284,100
AS13	India	07-07-2023	10-07-2023	1.5	169	47,790
AS14	India, Pakistan	14-06-2023	16-06-2023	1.5	7	175,925
AS15	Philippines	10-12-2022	23-01-2023	1.5	63	330,071
AS16	Oman, Yemen	23-10-2023	25-10-2023	0.5	1	9,000
AS17	Indonesia	18-09-2024	04-11-2024	0.5	18	1,100
AS18	Azerbaijan	12-10-2024	23-10-2024	0.5	2	67
AS19	Philippines	12-10-2024	23-10-2024	0.5	3	12,793
AS20	Sri Lanka	08-10-2024	10-10-2024	0.5	3	9,591
EU01	Spain	27-10-2024	04-11-2024	2.5	221	447
EU02	Bosnia and Herzegovina	03-10-2024	05-10-2024	1.5	14	-
EU03	Austria, Czech Republic, Germany, Poland, Romania, Slovakia	12-09-2024	18-09-2024	1.5	13	7,042
EU04	France	3-12-2023	03-01-2024	1.5	1	743
EU05	Germany	18-12-2023	03-01-2024	1.5	0	-

ID	Country	From Date	To Date	GDACS Score	Deaths	Displaced
EU06	Norway	31-10-2024	05-11-2024	0.5	0	98
EU07	Greece	04-09-2023	15-09-2023	0.5	20	4,506
EU08	Italy	16-10-2024	28-10-2024	0.5	1	290
EU09	Italy	17-09-2024	25-09-2024	0.5	0	1,550
EU10	France	01-10-2024	26-10-2024	0.5	1	347
EU11	Italy	30-10-2023	04-11-2023	0.5	10	510
EU12	Italy	01-05-2023	26-05-2023	0.5	17	36,450
EU13	Slovenia	03-08-2023	05-08-2023	0.5	3	4,000
EU14	United Kingdom	28-12-2023	01-01-2024	0.5	3	1,120
EU15	United Kingdom	19-10-2023	12-11-2023	0.5	1	1,620
EU16	Russia	01-07-2023	10-07-2023	0.5	0	407
EU17	Austria	03-08-2023	13-08-2023	0.5	1	57
EU18	Russia	11-08-2023	21-08-2023	0.5	8	2,500
EU19	Kosovo, Serbia	18-01-2023	22-01-2023	0.5	2	584
EU20	Italy	26-11-2022	10-12-2022	0.5	7	1,304
NA01	Dominican Republic	02-11-2024	04-11-2024	0.5	0	1,390
NA02	Costa Rica	06-11-2024	08-11-2024	0.5	1	155
NA03	United States	09-01-2024	03-02-2024	0.5	1	405
NA04	United States	16-08-2024	18-09-2024	0.5	1	55
NA05	Panama	29-09-2024	01-10-2024	0.5	1	12
NA06	Mexico	16-10-2024	22-10-2024	0.5	7	247
NA07	United States	22-12-2022	28-01-2023	0.5	4	500
NA08	Canada	01-07-2023	23-07-2023	0.5	0	1,270
NA09	United States	16-06-2023	24-08-2023	0.5	5	14,525
NA10	Honduras	03-11-2023	05-11-2023	0.5	4	1,024
NA11	Honduras	07-12-2023	09-12-2023	0.5	2	30
NA12	Cuba, Jamaica	03-11-2024	10-11-2024	0.5	0	38,095
NA13	Costa Rica	06-11-2024	08-11-2024	0.5	1	155
NA14	Mexico	30-08-2024	04-10-2024	0.5	18	92
NA15	United States	22-12-2022	28-01-2023	0.5	4	500
OC01	New Zealand	03-10-2024	05-10-2024	0.5	0	100
OC02	Australia	29-12-2022	05-01-2023	0.5	0	700
OC03	Fiji	03-02-2023	05-02-2023	0.5	1	350
OC04	New Zealand	12-02-2023	14-02-2023	0.5	0	3,810
OC05	Australia	01-01-2024	23-02-2024	0.5	0	286
OC06	Fiji	14-03-2024	16-03-2024	0.5	0	230
OC07	Papua New Guinea	25-03-2024	27-03-2024	0.5	4	2,250
OC08	Australia	22-10-2022	05-11-2022	0.5	2	540
OC09	New Zealand	11-11-2022	15-11-2022	0.5	0	200
SA01	Brazil	23-04-2024	17-05-2024	1.5	144	540,548
SA02	Brazil	23-05-2022	26-05-2022	1.5	92	16,619
SA03	Chile	20-06-2024	28-06-2024	0.5	0	1,500
SA04	Uruguay	20-03-2024	22-03-2024	0.5	0	4,687
SA05	Brazil	05-11-2024	08-11-2024	0.5	1	1,950
SA06	Brazil	19-12-2022	06-01-2023	0.5	3	242
SA07	Colombia	09-01-2023	17-01-2023	0.5	1	558
SA08	Brazil	17-01-2023	19-02-2023	0.5	5	4,900
SA09	Brazil	18-02-2023	20-02-2023	0.5	40	2,496
SA10	Peru	22-02-2023	01-03-2023	0.5	1	740

ID	Country	From Date	To Date	GDACS Score	Deaths	Displaced
SA11	Peru	16-01-2023	18-04-2023	0.5	24	2,045
SA12	Ecuador	22-05-2023	06-06-2023	0.5	3	46
SA13	Brazil	07-07-2023	11-07-2023	0.5	15	3,850
SA14	Chile	19-08-2023	21-08-2023	0.5	1	1,200
SA15	Argentina	26-11-2023	14-12-2023	0.5	2	2,340
SA16	Venezuela	08-10-2022	22-10-2022	0.5	61	-
SA17	Bolivia	10-02-2024	14-02-2024	0.5	2	420
SA18	Brazil	03-03-2024	05-03-2024	0.5	0	1,663
SA19	Peru	26-12-2023	12-03-2024	0.5	21	727
SA20	Argentina	03-03-2024	17-03-2024	0.5	3	1,194